Nature Communications

https://doi.org/10.1038/s41467-026-69264-9

Article in Press

Scalable solution soaking quenching technique unlocks efficient and durable wide bandgap perovskite solar modules

Received: 17 June 2025

Accepted: 29 January 2026

Cite this article as: Fang, Y., Sun, J., Tan, Y. *et al.* Scalable solution soaking quenching technique unlocks efficient and durable wide bandgap perovskite solar modules. *Nat Commun* (2026). https://doi.org/10.1038/s41467-026-69264-9

Yuxuan Fang, Jinglin Sun, Ying Tan, Guo Yang, Huanyu Chen, Mingwei Gu, Yongbin Feng, Meifang Yang, Hong Liu, Jun Fang, Congcong Wu, Longbin Qiu, Jin Ge, Zhibin Yang & Wu-Qiang Wu

Scalable solution soaking quenching technique unlocks efficient and durable wide bandgap perovskite solar modules

Yuxuan Fang[1], Jinglin Sun[2], Ying Tan[1], Guo Yang[1], Huanyu Chen[1], Mingwei Gu[1], Yongbin Feng[1], Meifang Yang[1, 3], Hong Liu[4], Jun Fang[5], Congcong Wu[4], Longbin Qiu[5], Jin Ge[1], Zhibin Yang[2], Wu-Qiang Wu[1]*

[1]Key Laboratory of Bioinorganic and Synthetic Chemistry of Ministry of Education, LIFM, School of Chemistry, IGCME, Sun Yat-Sen University, Guangzhou, 510275, P. R. China.

[2]School of Chemistry and Chemical Engineering, Shanghai Jiao Tong University, Shanghai 200240, P. R. China.

[3]School of Chemistry and Chemical Engineering, Yangzhou University, Yangzhou 225002, P. R. China.

[4]Key Laboratory for the Green Preparation and Application of Functional Materials, Hubei Key Laboratory of Polymer Materials, School of New Energy and Electrical Engineering, Hubei University, Wuhan 430062, China.

[5]Department of Mechanical and Energy Engineering, SUSTech Energy Institute for Carbon Neutrality, Southern University of Science and Technology, Shenzhen, 518055, China.

*Corresponding author: wuwq36@mail.sysu.edu.cn

Abstract

Wide-bandgap mixed-halide perovskite photovoltaic modules show strong potential for portable chargers, building-integrated photovoltaics, agrivoltaics, and tandem systems, but large-area processing exacerbates crystallization heterogeneity, surface defects, and halide phase segregation. Conventional spin-coating passivation fails to deliver uniform interfacial control at scale. Here, an industrially inspired solution-soaking quenching technique is introduced, in which hot blade-coated wide-bandgap perovskite films (~30 cm^2) are immersed in cold SrI_2/isopropanol. It enables rapid surface reconstruction and uniform surface passivation, enhances photoluminescence

uniformity, improves crystallinity, reduces roughness, and stabilizes halides via gradient Sr^{2+} incorporation. These effects mitigate tensile stress, optimize energy-level alignment, and suppress light-induced phase separation. Methylammonium-free wide-bandgap small-area (0.04 cm^2) devices achieve efficiencies up to 22.03%, while a 10.13 cm^2 module delivers 20.32% efficiency with excellent operational stability. The method is versatile across wide-bandgap perovskite compositions and enables practical applications including portable chargers, semitransparent modules (18.41% bifacial equivalent efficiency), and >27% efficient all-perovskite tandem windows.

Introduction

Perovskite solar cells (PSCs) have gained widespread research attention in the field of photovoltaics due to their remarkable power conversion efficiencies (PCEs) and low-cost manufacturing processes[1]. Recent advances demonstrated that small-scale laboratory PSCs (active area <0.1 cm^2) have achieved certified PCEs approaching 27%, which is comparable to the performance of commercial crystalline silicon solar cells[2]. Notably, by tailoring the bandgap properties of perovskite materials, functional devices can be designed for specific application scenarios. Among them, mixed-halide wide-bandgap (WBG) perovskite materials, owing to their larger bandgap (range: 1.6-2.0 eV), theoretically maintain higher optical transparency and achieve higher open-circuit voltage (V_{OC}), showing unique advantages in semi-transparent photovoltaic devices and tandem solar cells[3,4]. This offers promising potential for the development of next-generation photovoltaic technologies and products.

Currently, the mainstream WBG perovskite system predominantly adopts mixed-halide formulations with high bromine (Br) content. However, inherent issues such as differences in crystallization dynamics between different halides, halide phase segregation and ion migration induced by external factors (e.g., light, temperature, and moisture) lead to poor crystallization quality, significant chemical compositional inhomogeneity, and abundant bulk/surface defects in

perovskite thin films[5-7]. These drawbacks collectively cause severe interfacial non-radiative recombination and carrier transport losses, thereby constraining further improvements in efficiency and operational stability. Blade-coating, as a scalable large-area thin film deposition technique, has demonstrated considerable industrialization potential due to its low ink consumption and high compatibility with roll-to-roll processing[8]. However, during the blade-coating of large-area WBG perovskite films, the crystallization heterogeneity of mixed-halide components exacerbates the aforementioned uneven crystallization and abundant interfacial defects, resulting in the degradation of key photovoltaic parameters across the solar modules, ultimately leading to performance deterioration[9]. For instance, when scaling up high-efficiency small-area cells (<1 cm^2) to modules (>10 cm^2), a pronounced PCE roll-off exceeding 4% is often observed, posing a critical barrier to commercialization and practical development[10]. Notably, the reduction in fill factor (FF) induced by device scaling is more significant than the reductions in short-circuit current density (J_{SC}) and V_{OC}[11-13]. This phenomenon is primarily attributed to the amplification effect of interfacial imperfections, inhomogeneous carrier transport paths, and accelerated degradation of interfacial properties at larger scales, which collectively lead to a significant increase in series resistance (R_S) at the interfaces[14,15].

Studies have demonstrated that introducing organic/inorganic small molecules or modifying the interface between the perovskite layer and the electron transport layer (ETL) can optimize the interfacial contact and enhance charge extraction dynamics, thereby improving the J_{SC} and FF of PSCs[16-18]. For example, Liu et al. sequentially deposited ethylenediamine diiodide ($EDAI_2$) and 4-fluoro-phenethylammonium chloride (4F-PEACl) to improve the interfacial contact between perovskite and the C_{60} ETL, effectively alleviating interfacial energy losses and enhancing charge extraction efficiency, achieving a breakthrough in the performance of WBG perovskite/silicon tandem solar cells[19]. Similarly, Jiang et al. used cyclohexane 1,4-diammonium diiodide ($CyDAI_2$) as an interfacial passivation material, successfully suppressing defect states at the WBG perovskite/ETL interface, significantly reducing interfacial recombination and enhancing PCE,

achieving an outstanding efficiency of 26.4% in WBG perovskite/organic tandem solar cells[20]. However, conventional interface modification strategies for PSCs and modules mainly rely on spin-coating, which is limited by solvent evaporation-induced convention effects (i.e., the well-known coffee-ring effect), resulting in uneven distribution of the modification solution and aggregation of additives at the edges of perovskite films[21,22]. As the device area increases, this phenomenon becomes more pronounced, making it difficult to precisely control the spatial distribution of modifying ions. This unevenness often leads to localized chemical composition variations on the film surface, which in turn adversely affects surface optoelectronic properties such as charge transport efficiency. The spatial heterogeneity at the interface severely disrupts the uniformity of charge transport, becoming a critical bottleneck for the scalable fabrication of high-performance photovoltaic modules. Furthermore, methylammonium cations (MA^+), widely used in WBG perovskite system, suffer from thermal instability, severely limiting outdoor applications. The high volatility of MA^+ at elevated temperatures easily triggers phase separation and defect proliferation, leading to structural degradation[23,24]. Studies have shown that MA^+-driven crystallization disorders resulted in more grain boundaries and interfacial defects[25,26]. Therefore, it is highly desirable and imperative to develop simple, scalable and universal post-treatment methods to enhance surface chemical homogeneity, optimize interfacial contact, suppress interfacial defect states, and improve interfacial charge transport efficiency, which is of great significant for advancing the performance of large-area WBG photovoltaic devices.

Inspired by traditional manufacturing processes, the quenching technique used in rapid cooling of hot-processed metal materials can effectively improve material performance. By precisely controlling the cooling rate, this technique enhances material hardness and strength while relieving stress and thermal deformation, making it a key process in modern industrial manufacturing[27,28]. In this work, we innovatively introduce industrial quenching technology into the photovoltaic field for post-treatment of large-area perovskite films to enhance their optoelectronic performance. Specifically, a quenching medium based on cold SrI_2/IPA solution is developed for rapid soaking

treatment of hot perovskite films. This approach achieves uniform and efficient surface/interface modification of large-area perovskite films at the macroscopic scale. This cold and hot shock-driven surface reconstruction strategy substantially enhances the crystallinity of the films and reduces surface roughness by 53%. Simultaneously, through gradient doping of metal ions from film surface to bulk interior, coupled with halide stabilization, the crystallization-induced tensile stress is effectively relieved, energy level alignment is optimized, and the surface homogeneity and interfacial charge transport efficiency of large-area films are significantly enhanced. The solution-soaking quenching (SSQ) technique demonstrates universal compatibility, effectively treating various mainstream WBG compositions and realizing the synergistic integration of multifunctional organic solutes in the quenching medium. Notably, the optimized blade-coated small-area (0.04 cm^2) devices with bandgaps of 1.65 eV, 1.68 eV, and 1.78 eV attain remarkable PCEs of 22.03%, 21.39%, and 18.66%, respectively. The SSQ strategy is suitable for other MA-free perovskite systems with different bandgaps, validating the universality of this approach. After scaling up to large-area modules, the enhanced chemical uniformity of surface modification/passivation molecules dramatically enhances the photoluminescence (PL) intensity and simultaneously reduces the coefficient of variation in fluorescence intensity from 17.16% to 0.67%, effectively solving the scaling-up problem while retaining the high efficiency and stability characteristics validated in small-area devices. This optimization results in a 63% reduction (from 17.45 Ω to 6.52 Ω) in overall R_S, thereby significantly boosting the FF of the WBG perovskite solar modules (PSMs) from 69.95% to 80.44%. Ultimately, the champion PCEs of 20.32% (active area: 10.13 cm^2) are achieved, representing one of the highest reported values for such type of devices. Encapsulated MA-free PSMs exhibit remarkable thermal stability, retaining 87% of their initial PCE after 550 h of thermal aging at 65 °C according to the ISOS-D-2I protocol. In addition, encapsulated devices maintain more than 96% of their initial PCE after over 1,000 h of continuous maximum power point (MPP) tracking under the ISOS-L-1 standard at room temperature (25 °C) and 50-60% relative humidity, demonstrating superior stability compared to most solution-

processed WBG perovskite devices[29,30]. Furthermore, this technology is successfully extended to diverse application scenarios, such as semi-transparent WBG PSMs suitable for agricultural photovoltaics (a bifacial equivalent efficiency of 18.41%, 17.55% average visible light transmittance (AVT)) and four-terminal switchable all-perovskite tandem photovoltaic windows for building-integrated photovoltaic windows (translucent mode: 17.22% PCE; opaque maximal energy harvesting mode: 27.12% PCE), as well as portable charging devices. By overcoming the core challenge of large-area perovskite film post-treatment uniformity, this study provides a practical technical solution to simultaneously enhance device performance and scalability. These advancements highlight the potential of perovskite photovoltaics to expand into commercial applications and adapt to diverse application scenarios, bridging the gap between laboratory innovations and industrialization requirements.

Results

Surface homogenization in large-scale perovskite films

In modern industry, quenching technology rapidly cools metals that have been heated to high temperatures, which helps homogenize their surface and increase surface hardness. Precisely controlling the temperature differences between hot and cold, as well as cooling rate, can optimize the microstructure and generate compressive stress that inhibits crack formation, significantly enhancing the material's durability. This process has become a core technique in precision industries such as aerospace and automotive manufacturing. Inspired by this industrial metallurgical approach, we have innovatively implemented a quenching-like post-treatment strategy by quickly cooling large-area perovskite films with cold quenching solution (Fig. 1a), in order to enhance their surface homogeneity and optoelectronic performance. As a case study, this research first focused on mixed-halide WBG ($FA_{0.8}Cs_{0.2}Pb(I_{1-x}Br_x)_3$) perovskite films. Specifically, the blade-coated perovskite films were immediately soaked in a 5 °C SrI_2/isopropanol (IPA) quenching medium after conventional thermal annealing at 105 °C, rather than cooling naturally

(see the detailed experimental details in Methods section). The inherent thermodynamic instability of the initial film is activated by the kinetic shock of quenching, guided by the chemical potential gradient of the solution, and subsequently stabilized through the thermal energy of the final annealing tempering step, ultimately resulting in gradient doping and comprehensive surface reconstruction (Supplementary Fig. 1). This controlled rapid cooling process simultaneously achieved gradient doping of Sr^{2+} from the surface to the bulk interior of the film (will be discussed later), along with grain boundary reconstruction, thereby enhancing the structural toughness of the crystals and effectively suppressing grain boundary defect formation.

Scanning electron microscope (SEM) analysis (Fig. 1b) revealed that the control blade-coated WBG perovskite film exhibited a polycrystalline structure with obvious voids between adjacent grains and uneven grain size distribution, accompanied by an atomic force microscopy (AFM)-measured root mean square (RMS) roughness of 13.2 nm (Supplementary Fig. 2). These undesirable morphological features were prone to the formation of deep-level defect states, which, acted as Shockley-Read-Hall recombination centers, substantially exacerbated carrier loss and reduced carrier lifetimes. In contrast, the SSQ-derived films demonstrated remarkable morphological improvement (Fig. 1c), with densely interlocked grains and a 53% reduction in surface roughness (a RMS of 6.2 nm, Supplementary Fig. 3). To quantitatively substantiate these morphological and crystallographic improvements, statistical analysis of grain sizes distribution from relatively larger-area regions of SEM images was conducted. As depicted in Supplementary Fig. 4, the SSQ-treated perovskite film exhibited more uniform grain size distribution, with the average grain size increasing from 224.1 nm for the control to 242.3 nm. Furthermore, XRD patterns collected from five distinct regions of the large-area (5.2 cm × 6.0 cm) SSQ-treated film showed virtually similar perovskite characteristic peaks without any detectable secondary phases/impurities (Supplementary Fig. 5 and 6), demonstrating excellent phase purity and uniformity across a large-area dimension. These quantitative data unequivocally confirmed that the SSQ treatment indeed promoted the growth of more uniform and high-quality perovskite films

with enhanced crystalline properties, which underpinned the improved photovoltaic performance. This improvement is attributed to solvent-mediated surface etching in the quenching solution and passivation molecule-assisted surface reconstruction caused by the cool-thermal shock. Notably, when using the same SrI_2/IPA solution, under the same temperature difference conditions, the spin-coated (SC) post-treatment merely reduced the roughness to 11.6 nm (Supplementary Fig. 7 and 8). This limitation originates from Marangoni convection during the conventional spin-coated post-treatment, where differential solvent evaporation rates on the wet-film surface creates radial temperature and concentration gradients, leading to solute accumulation at the droplet edges (coffee-ring effect). Such inhomogeneous deposition hinders uniform surface reconstruction and induces localized chemical heterogeneity. This effect becomes more pronounced as the film area increases, causing discontinuities in carrier transport channels and large interfacial charge transport barriers. In contrast, our SSQ technique completely circumvents this issue by immersing the entire film into the quenching solution, thereby eliminating the convective flows-induced coffee-ring effect and non-uniformities. This ensures a homogeneous and isotropic supply of SrI_2 across the entire film surface, guaranteeing uniform surface morphology and comprehensive defect passivation, showing a decisive advantage for scalability.

To systematically evaluate the scalability of the SSQ strategy, we extended the spatial homogeneity analysis to blade-coated WBG perovskite films of different dimensions (1.5 cm × 1.5 cm, 3.5 cm × 3.5 cm and 5.2 cm × 6.0 cm) and performed spatially resolved photoluminescence (PL) mapping tests on 5, 7 and 13 designated regions, respectively. For the perovskite films of different size dimensions, both SC and SSQ post-treatments effectively enhanced the PL intensity. One could notice the PL intensity of SC-treated films always decreased at the edges, as compared to the central region, leading to strong spatial nonuniformity, regardless of film areas. As the film area increased to 5.2 cm × 6.0 cm, such limitation of the SC method became more evident. In comparison, the SSQ-treated films maintained exceptional PL uniformity across all regions and all film sizes (Supplementary Fig. 9 and 10, Fig. 1d-e). Typically, for the largest-area WBG perovskite

film (5.2 cm × 6.0 cm) tested on 13 designated regions, the PL intensity of the central region (Region 7) showed the same enhancement trend as the small-area samples (Fig. 1e, Supplementary Fig. 11), with substantially amplified PL intensity after SrI_2/IPA post-treatment. Bright-field microscopy imaging (Fig. 1f) and confocal PL mapping images (Fig. 1g-i) revealed that in the SC post-treated films, the PL intensity of the edge region decreased by ~40% compared to the central region, primarily due to the significant central-to-edge gradient in modified ion distribution, where excessive SrI_2/IPA accumulated at the edges, leading to elevated non-radiative recombination centers. In stark contrast, the SSQ-derived films demonstrated exceptional surface homogeneity over a large-scale, with the coefficient of variation (CV) of PL intensity reduced from 17.16% (SC film) to 0.67%. This improvement in surface passivation uniformity resulted from selective etching at the solid-liquid interface mediated by the quenching solvent and passivation ions-assisted surface reconstruction and localized structural reorganization. The synergistic optimization of morphological homogenization and uniform surface defect passivation is expected to improve interface contact and charge transport performance with other functional layers, providing a scalable solution for the fabrication of high-performance large-area perovskite optoelectronic devices.

Halide homogenization and stabilization

The nucleation and crystallization dynamics of blade-coated perovskite precursors are fundamentally governed by the synergistic interplay between thermodynamic driving forces (e.g., supersaturation) and kinetic constraints (e.g., solvent evaporation rate). As illustrated in Fig. 2a, during blade-coating, solvent evaporation driven by surface tension at the air-liquid interface induces preferential surface-initiated crystallization of the wet film, resulting in a top-down crystallization mechanism[31,32]. In WBG perovskites, the use of mixed-halide compositions introduces additional complexity due to varying reactivity and volatility of halide components. As a result, the spatial heterogeneity in chemical composition emerges, leading to pronounced halide

segregation and the formation of abundant halide vacancies[33,34]. Under sustained light exposure or thermal stress, this segregation worsens, producing s I-rich and Br-rich domains that serve as trap centers for photogenerated carriers[35]. This amplifies non-radiative recombination and causes significant open-circuit voltage (V_{OC}) losses[36]. More critically, this undermines the operational stability of WBG PSCs[37]. Mechanistically, the smaller ionic radius of Br^- facilitates its preferential migration through vacancy-mediated pathways, exacerbating phase separation (Fig. 2b). This effect intensifies with increasing bromine content in the perovskite formulation[38]. Surface treatment strategies, particularly those involving customized passivation layers or buffer interfaces, have shown promise in regulating halide distribution (e.g., via halide compensation) and suppressing ion migration (Fig. 2c)[39,40]. However, conventional solution-coating treatments typically only modify the top surface of the perovskite film, offering minimal stabilization of halide ions in the bulk or at the bottom interface.

To probe the effectiveness of different surface treatments, we performed depth-profile analysis using time-of-flight secondary ion mass spectrometry (ToF-SIMS) on perovskite films treated with SrI_2/IPA SC and SrI_2/IPA SSQ, respectively. As shown in Figs. 2d and 2e, both treatments successfully introduced Sr^{2+} into the film and modulated halide distribution. Sr^{2+} ions (ionic radius of 1.118 Å) from the halide salt could partially substituted Pb^{2+} (ionic radius of 1.190 Å), as is verified by consistent shift of diffraction peaks to higher angles in XRD patterns owing to lattice contraction (Supplementary Fig. 12), preferentially coordinated with halide ions (Br^-, I^-), stabilizing them and suppressing their migration, while also filling halide vacancies[41-43]. To directly probe the surface chemical modification and iodine vacancy compensation induced by the SSQ treatment, we performed X-ray photoelectron spectroscopy (XPS) on both control and SrI_2/IPA SSQ-treated perovskite films, providing quantitative information on surface I/Pb atomic ratios. Survey XPS spectra for these two samples were shown in Supplementary Fig. 13a. For the mixed-halide $FA_{0.8}Cs_{0.2}Pb(I_{0.8}Br_{0.2})_3$ perovskite compositions, the theoretical I/Pb ratio is 2.4. However, the average I/Pb ratio measured on the surface of the control perovskite film was only

2.07, revealing a pronounced iodine-deficient surface characteristic. After SrI_2/IPA SSQ treatment, the surface I/Pb ratio exhibited a remarkable increase to 2.26 (Supplementary Fig. 13b). Even considering the potential partial substitution of Pb^{2+} by Sr^{2+}, the adjusted I/(Pb+Sr) ratio still reached ~2.24, which remained substantially higher than that of the control film. This unambiguously demonstrated that the SSQ treatment effectively mitigated surface iodine loss by supplying additional iodide ions from the quenching medium, thereby filling undesirable iodine vacancies[39,44]. Notably, the spin-coated treatment limits Sr^{2+} penetration depth, resulting in a gradient in mixed-halide ion concentrations, decreasing from top down, which fostered inhomogeneous halide distribution and I/Br-enriched domains formation, compromising film uniformity. In contrast, films treated via SSQ exhibited more uniform halide distribution across both the bulk and interfaces. This improvement was attributed to the unique cold/thermal shock mechanism of the SSQ process. During perovskite lattice expansion, Sr^{2+} penetrated deeply, and the subsequent rapid cooling locked more portions of Sr^{2+} ions within the lattice, forming stable Sr-halide complexes through chemical bonding. These complexes acted as structural bridges that relieve lattice stress (further discussed later), effectively suppressing halide ion migration and phase segregation. This comparison highlighted the critical role of SSQ strategy in achieving halide homogenization throughout the WBG perovskites. To unravel the kinetics of Sr^{2+} incorporation, we monitored the evolution of passivation by measuring the PL intensity from both the front and rear sides of the film after quenching and during subsequent tempering (Supplementary Fig. 14). The front-side PL intensity increased immediately after quenching, and saturated after 80 s, indicating rapid surface passivation. In contrast, the rear-side PL intensity remained low without tempering and increased gradually upon annealing, saturating after ~100 s. This delay demonstrated that Sr^{2+} doping occurred via a time-dependent, solid-state diffusion process during tempering, enabling the passivating species to propagate from the surface into the bulk, thereby achieving comprehensive film improvement.

To evaluate the thermal stability of WBG perovskite materials, we conducted temperature-dependent photoluminescence (PL) measurements. As shown in Supplementary Fig. 15, PL intensity of all three perovskite films decreased with rising temperature, primarily due to exciton dissociation into free carriers, which preferentially underwent non-radiative recombination via defect states or lattice vibrations[45]. For the control perovskite, PL intensity dropped by 50% between 140 K-160 K. In contrast, the SrI_2-quenched sample demonstrated substantially mitigated thermal-induced fluorescence-quenching behavior, maintaining relatively high PL intensity up to 300 K. This improvement in thermal stability was attributed to the uniform incorporation of Sr^{2+} halide salts during post-treatment, which effectively passivated halide vacancies at both surfaces and in the bulk, stabilizing the lattice and suppressing defect-assisted non-radiative recombination. In-depth analysis of normalized PL spectra from 100-320 K (Figs. 2f-h) revealed distinct temperature responses. The control film exhibited progressive PL broadening (increased full width at half maximum, FWHM) and blue shifts with increasing temperature, signatures of intensified exciton-phonon coupling and thermally-induced halide segregation (Supplementary Fig. 16). While the SrI_2/IPA SC-treated film showed temperature-independent FWHM, the overall narrowing was modest, reflecting the dominance of surface passivation with limited bulk effect, and a trade-off with thermally activated broadening. In contrast, the solution-soaked, quenched film displayed a narrower FWHM at 320 K (32 nm *vs.* 41 nm for control), indicating a robust crystal structure reinforced by surface reconstruction and structural rearrangement. This was enabled by synergistic passivation of both surface and bulk defects, effectively mitigating thermally induced lattice distortion and phase segregation. Such temperature-insensitive PL characteristics and enhanced optoelectronic homogeneity underscored a promising pathway toward high-performance perovskite-based optoelectronic devices through comprehensive defect passivation and structural stabilization strategies. Additionally, the dynamics of light-induced halide segregation and phase separation were monitored via time-resolved in-situ photoluminescence (PL) spectroscopy. Different wide-bandgap perovskite films were subjected to

continuous irradiation under ambient atmospheric conditions. As shown in Supplementary Fig. 17, the PL peak of the control film, initially centered at 748 nm, exhibited a pronounced redshift over 20 min of light exposure light exposure, accompanied by a broadening of FWHM to 47.03 nm. This spectral evolution indicated the formation and accumulation of lower-bandgap (I-rich) perovskite domains, which may promote non-radiative carrier recombination across phase-segregated regions[46,47]. In stark contrast, the SSQ-treated mixed-halide WBG perovskite films showed negligible peak shift and FWHM broadening under identical conditions, with only a minor decrease in PL intensity. These results highlighted the effectiveness of the SSQ technique in mitigating light-induced halide segregation and maintaining phase stability in mixed-halide WBG perovskites.

Surface reconstruction and residual stress mitigation

We directly visualized the vertical morphological features of the WBG perovskite films using cross-sectional SEM characterization. As shown in Supplementary Fig. 18a, the untreated control film exhibited pronounced voids between adjacent grains. These voids are primarily attributed to incomplete solvent evaporation during crystallization, which constrained the grain growth and resulted in a higher density of grain boundaries and related defects. Such morphological features not only introduce non-radiative recombination centers but also provide diffusion pathways for moisture, oxygen and mobile ions, thereby accelerating device degradation. In stark contrast, the SrI_2/IPA SSQ-treated film displayed a tightly packed grain structure (Supplementary Fig. 18b), confirming that the SSQ post-treatment effectively promoted grain fusion and film densification, consistent with surface SEM observations (Fig. 1b and c) discussed earlier. This optimized morphology significantly reduced the number of grain boundaries and the overall defect density. The resulting compact microstructure is beneficial for efficient charge transport and serve to suppress environmentally-induced degradation pathway, laying a robust foundation for enhanced device efficiency and operational stability. To further assess the crystalline and structural quality

across the film thickness, we performed depth-resolved grazing-incidence wide-angle X-ray scattering (GIWAXS) measurements. By systematically tuning the incident angle (2°, 1.5°, and 1°) to modulate the X-ray penetration depth, we evaluated the depth-dependent crystallinity of the perovskite films from the top surface to the bottom interface[48]. As shown in Fig. 3a-i, the control film exhibited weak surface diffraction signals that rapidly attenuated with increasing depth, reflecting poor overall crystallinity and pronounced spatial inhomogeneity in crystal quality. In comparison, the SrI_2/IPA SSQ-treated film displayed significantly enhanced diffraction intensity and sharper Debye-Scherrer rings under higher incidence angles (2°), corresponding to the surface-sensitive region. This observation highlighted the markedly improved surface crystallinity achieved through quenching. Notably, even at reduced incidence angles of 1.5° and 1°, which probe deeper regions of the film, the SrI_2/IPA SSQ-treated sample consistently exhibited the strongest diffraction signals among all three groups. In contrast, the SrI_2/IPA SC-treated film showed a noticeable signal drop at 1°, with intensities approaching those of the untreated control. These comparative results reaffirmed that the conventional SrI_2/IPA spin-coating treatment predominantly improved crystallinity near the film surface but failed to enhance the bulk crystal quality. Conversely, the SrI_2/IPA SSQ approach enabled solution-mediated surface reconstruction and structural reorganization driven by the cooperative effects of solute and solvent. This process uniformly enhanced crystallinity throughout the entire film thickness, from the top surface to the buried interface, achieving a comprehensive improvement in film structure. The optimized morphology and enhanced crystallinity achieved by the SSQ treatment are expected to directly benefit the optoelectronic properties of the perovskite films. As shown in Supplementary Fig. 19, the SSQ-treated film exhibited significantly stronger light absorption capability than that of the control film, establishing a solid foundation for generating higher photocurrent in the complete PSCs (will be discussed in the following section).

Residual stress naturally arises in thin-film materials and devices during fabrication, processing, and operation. This stress primarily originates from mismatches in thermal

expansion coefficients between the substrate and the film, lattice mismatches, structural defects such as vacancies, and process-related factors like solvent evaporation and cooling rates[49-51]. Notably, residual tensile stress can cause lattice expansion, weaken chemical bonds, and reduce the formation energy of defects. These changes exacerbate non-radiative carrier recombination, severely comprising the optoelectronic performance of perovskite materials and devices[52]. Moreover, tensile strain can elongate ion diffusion paths, facilitate ion migration, and accelerate phase segregation and interfacial corrosion. Such phenomena would be further intensified under light, heat and moisture, thus posing a significant threat to device stability[53]. In large-area perovskite films, uneven thermal conduction across the substrate can generate temperature gradients (e.g., rapid cooling at the edges versus thermal retention at the center), inducing nonuniform thermal expansion and contraction. This results in macroscopic stress zones, typically compressive at the edges and tensile at the center[54,55]. Such spatially heterogeneous stress distributions magnified the effects of residual stress in large-area perovskite thin films, limiting both the efficiency and long-term stability of large-scale perovskite photovoltaic modules.

We systematically investigated the residual stress (δ_R) in the control, SrI_2/IPA SC-treated, and SrI_2/IPA SSQ-treated WBG perovskite films using grazing incidence X-ray diffraction (GIXRD). The measurements were conducted at a fixed 2θ angle while varying the instrument tilt angels (Ψ), maintaining consistent penetration depth (Figs. 3j-l). The δ_R was calculated from the linear plot of 2θ as a function of $\sin^2\Psi$, according to the stress equation:

$$\delta_R = -\left(\frac{E}{2(1+v)}\right)_{\{hkl\}} \frac{\pi}{180} \cot\theta_0 \frac{\partial(2\theta)}{\partial(\sin^2\psi)} \quad (1)$$

where E represents the Young's modulus (17.8 GPa for perovskites), v represents the Poisson's ratio (≈0.33), and θ_0 represents half of the scattering angle $2\theta_0$ for stress-free perovskite[56]. The XRD signal at 32.1° corresponded to (210) facet of perovskite film was chosen for analysis, which minimized orientation effects and provided more reliable information on structure symmetry[52]. For the control film, the diffraction peaks shifted progressively toward lower 2θ values as Ψ

increased from 5° to 45° (Fig. 3j), indicating a monotonic increase in crystal plane distance of (210) facet, clear evidence of the presence of residual tensile stress within the perovskite film. Fitting the 2θ as a function of $\sin^2\Psi$ yielded a δ_R of 51.76 MPa. In contrast, the SrI_2/IPA SC-treated film showed reduced peak shifts and a lower δ_R of 44.68 MPa. The SrI_2/IPA SSQ-treated film exhibited the smallest peak shift and a further reduced slope (-0.09) in the fitted curve, corresponding to the lowest δ_R of 36.83 MPa (Figs. 3m and 3n). This stress relief was attributed to surface reconstruction and lattice reorganization mediated by the SrI_2/IPA soaking and quenching process. Specifically, the substitution of Pb^{2+} by Sr^{2+} allows for subtle lattice adjustments due to their similar ionic sizes but differing bonding characteristics, alleviating lattice mismatch and modulating internal stress. On one hand, Sr^{2+} doping could introduce compensatory compressive stress through stronger halide bonding or localized lattice contraction. On the other hand, Sr^{2+} could stabilize halide ions, reducing defect-induced lattice distortion and associated elastic strain energy. Unlike surface-limited spin-coating, the quenching post-treatment facilitated deeper infiltration of SrI_2/IPA into grain boundaries and voids, triggering localized dissolution-recrystallization. This promoted grain fusion and interfacial smoothing, effectively releasing interfacial strain.

These findings demonstrated that SrI_2/IPA-assisted SSQ post-treatment synergistically enhanced film quality by enabling smooth, dense perovskite growth, mitigating lattice mismatch, and relieving residual stress through compositional engineering (Sr^{2+} doping and halide compensation) and surface reconstruction. Consequently, this strategy significantly improved the mechanical robustness and environmental resilience of perovskite films, extending the operational lifespan of corresponding optoelectronic devices.

Energy level modulation and carrier dynamics optimization

Surface treatments can markedly influence the surface electronic properties of perovskite films. To investigate the impact of SrI_2/IPA post-treatments on the surface energy levels of WBG

perovskite films, we performed ultraviolet photoelectron spectroscopy (UPS) measurements. By calculating the energy difference between the incident *He I* photon energy (21.22 eV) and the binding energy corresponding to secondary electron cut-off edge as shown in Supplementary Fig. 20, the Fermi level (E_F) of the perovskite films can be calculated. As shown in Fig. 4a, the E_F uplifted from -4.37 eV for the control sample to -4.32 eV for the SrI_2/IPA SC film, and further to -4.26 eV for the SrI_2/IPA SSQ film. This result indicated that the SrI_2/IPA post-treatment, particularly the quenching process, elevated the E_F closer to the conduction band (CB), characteristic of n-type doping. This trend aligns well with previous reports on meatal halide salt treatment, which suggested simultaneous electron and defect compensation effects leading to beneficial doping behavior[57]. Considering the WBG perovskite's bandgap of 1.68 eV (discussed later) and the UPS-derived valence band (VB) positions, we found that the SrI_2/IPA quenching process also induced a slight downward shift in the CB. Combined with the favorable band bending induced by n-type doping, this adjustment reduced the energy barrier at the perovskite/electron transport layer (ETL) interface, facilitating more efficient interfacial electron extraction and thus enhancing device performance.

To probe the ultrafast carrier dynamics within the device and at relevant interfaces, we further conducted femtosecond transient absorption (fs-TA) spectroscopy on semi-devices with the layer-stacked architecture of ITO/PTAA/2PACz/perovskite with or without SrI_2/IPA treatment/C_{60} (Fig. 4b). Photoinduced charge transfer typically occurs over sub-picosecond to nanosecond timescales. By varying the pump-probe delay time and tracking changes in transient absorption (ΔA), we captured the dynamic behavior of excited-state carriers over time, revealing their relaxation into lower energy states. As shown in the fs-TA contour maps (Fig. 4c and d), both the control and SrI_2/IPA SSQ-treated semi-devices exhibited prominent ground-state bleaching (GSB) peaks near 740 nm. The decay rate of the GSB signal reflects the efficiency of photogenerated carrier extraction from the perovskite layer to adjacent charge transport layers. Compared to the control, the SrI_2/IPA SSQ-treated samples showed significantly faster GSB signal decay, indicating more

efficient carrier extraction. This rapid GSB decay suggested a swift depletion of photogenerated carriers, effectively reducing recombination probabilities and shortening the duration of ground-state bleaching. This improvement can be attributed to enhanced crystallinity, improved interfacial chemical homogeneity, and optimized energy level alignment resulting from the SrI_2/IPA SSQ treatment, which collectively, promoted directional carrier migration.

Time-resolved TA spectra (Fig. 4e and f) further corroborated this conclusion. At identical delay times, the SrI_2/IPA SSQ-treated semi-device exhibited flatter GSB peak signals, as compared to that of the control, indicating a shorter carrier residence time. The decay kinetics of GSB were analyzed via bi-exponential fitting according to the equation:

$$\tau_{\mathrm{avg}} = \frac{A_1\tau_1{}^2 + A_2\tau_2{}^2}{A_1\tau_1 + A_2\tau_2} \quad (2)$$

where A_1 and A_2 are the amplitudes of the fast and slow decay components, respectively. τ_1 and τ_2 represent the time constants for fast and slow decay components, respectively[58,59]. The results revealed a significantly reduced decay lifetime for the SrI_2/IPA SSQ-treated sample (303.3 ps) compared to the control (779.2 ps) (Fig. 4g and Supplementary Table 1). This outcome provided additional evidence that the SrI_2/IPA quenching process synergistically improved carrier dynamics through crystallization control, interface modification, and energy level optimization. Altogether, these enhancements enabled more efficient charge transfer and collection at the perovskite/charge transport layer interfaces, mitigating interfacial non-radiative recombination losses. As a result, the photocurrent output and fill factor are expected to be improved, underscoring the critical role of this post-treatment strategy in boosting the photovoltaic performance of PSCs.

Photovoltaic performance and stability

To evaluate the effect of the SSQ strategy on the photovoltaic performance of blade-coated MA-free WBG PSCs, we fabricated the devices with the structure of ITO/PTAA/2-PACz/$FA_{0.8}Cs_{0.2}Pb(I_{(1-x)}Br_x)_3$ perovskite with or without SSQ/C_{60}/bathocuproine (BCP)/Ag (Fig. 5a). Figure 5b compares the current density-voltage *(J-V)* characteristics of the PSCs without or

with SrI_2/IPA SSQ post-treatment, with corresponding photovoltaic parameters summarized in Table 1. Under simulated AM 1.5G one-sun irradiation (100 mW cm^{-2}), the control device yielded a reverse-scan power conversion efficiency (PCE) of 16.91%, with a short-circuit current density (J_{SC}) of 19.90 mA cm^{-2}, open-circuit voltage (V_{OC}) of 1.18 V, and fill factor (FF) of 72%, while the average PCE was 14.97% ± 0.84%. In contrast, devices treated with SrI_2/IPA SSQ exhibited a substantial improvement in PCE. The champion device achieved a PCE of 21.39%, with a V_{OC} of 1.21 V, J_{SC} of 21.68 mA cm^{-2}, and *FF* of 81.26%, showing negligible hysteresis. This represents one of the highest reported efficiencies for small-area WBG (~1.68 eV) PSCs fabricated via blade-coating (Supplementary Table 2). The forward-scan PCE was 20.94% (V_{OC} = 1.20 V, J_{SC} = 21.46 mA cm^{-2}, FF = 81.30%), and the average PCE was 20.28% ± 0.54%. In comparison, the SrI_2/IPA SC devices merely reached a PCE of 20.03% (FF=78%), which could be attributed to moderate modification effect induced by such surface-only treatments (Supplementary Fig. 21). This contrast underscores the superior performance enhancement enabled by the soaking-quenching approach.

Notably, SSQ treatment performed at 5 °C helped to realize the optimal device photovoltaic performance (Supplementary Fig. 22 and Supplementary Table 3), which can be attributed to sufficient cold-thermal shock to drive favorable surface reconstruction. The SrI_2/IPA concentration was optimized from 0.05 mg mL^{-1} to 0.50 mg mL^{-1}, with 0.20 mg mL^{-1} yielding the best device photovoltaic performance (Supplementary Fig. 231 and Supplementary Table 4). Particularly, the versatility of the SSQ approach is confirmed by employing $EDAI_2$/IPA as the quenching medium, which also yielded a high PCE of 20.21% (Supplementary Fig. 24), indicating that the SSQ post-treatment is applicable to other salts beyond SrI_2. The steady-state output of the best-performing SrI_2/IPA SSQ-treated device was shown in Fig. 5c, exhibiting a stabilized PCE of 21.05% over 120 s at the maximum-power-point of 1.05 V. External quantum efficiency (EQE) measurements corroborated the enhanced J_{SC}. Compared to the control, the SrI_2/IPA SSQ-treated PSC exhibited remarkably enhanced EQE across the 300-750 nm spectral range (Fig. 5d). The integrated current

density derived from EQE spectrum (i.e. 20.61 mA cm^{-2} for SrI_2/IPA SSQ-treated PSC *vs.* 19.07 mA cm^{-2} for the control PSC) was in good accordance with the *J-V* results, showing a discrepancy <5%.

EQE-based bandgap analysis (Supplementary Fig. 25) indicated the bandgap remained unchanged at 1.68 eV after quenching treatment. The decline in EQE at longer wavelengths is attributed to Urbach tail states caused by structural defects, impurities, and lattice dislocation[60]. The Urbach energy (E_U) can be calculated from the EQE spectra using the following equation: $\alpha = \alpha_0 \exp(\frac{hv}{E_U})$ (3)

in which α is the absorption coefficient, α_0 is a constant and hv is the photon energy (E)[61]. A reduction in E_U (23.32 meV *vs.* 24.58 meV), confirmed that the quenched films exhibited reduced lattice disorder, fewer defects, and improved energetic uniformity. The overall enhancement in device performance was attributed to concurrent improvements across all photovoltaic parameters. The increases in J_{SC} and FF stemmed from enhanced crystallinity, improved conductivity, better compositional homogeneity, and more efficient interfacial carrier extraction and transport. The enhancement of V_{OC} by ~30 mV was primarily due to suppressed trap-assisted recombination, resulting from a reduced defect density. To probe the origin of the FF enhancement, illumination intensity-dependent photoluminescence quantum yield (PLQY) measurements and quasi-Fermi level splitting (QFLS) analyses (from 0.001 to 2 suns) were performed (Supplementary Fig. 26). The SrI_2/IPA SSQ-treated film exhibited a steeper increase in PLQY, consistently higher absolute PLQY values across all measured illumination intensities, and lower ideality factor (n_{id}) (i.e. 1.38 *vs.* 1.41 for the control), demonstrating suppressed defect-assisted non-radiative recombination and more ideal diode behavior[62,63]. We concluded that reduced non-radiative recombination, together with both improved film quality and optimized energy-level alignment, collectively contributing to the significantly improved FF.

To quantify trap density and carrier mobility, we fabricated electron-only devices (ITO/SnO_2/perovskite (with or without SrI_2/IPA SSQ)/C_{60}/BCP/Cu) for space-charge-limited-

current (SCLC) measurements (Figs. 5e-f). The trap densities (N_{trap}) were derived from the trap-filled limit voltage (V_{TFL}) via the following equation:

$$N_{\text{trap}} = \frac{2V_{\text{TFL}}\varepsilon_0\varepsilon_{\text{r}}}{qL^2} \quad (4)$$

where ε_0, ε_r and L represented the vacuum permittivity, dielectric constant permittivity and film thickness (≈220 nm) of the perovskite film, respectively. As a result, the SrI_2/IPA SSQ-treated device exhibited a smaller V_{TFL} (0.18 V) and N_{trap} (1.32×10^{16} cm^{-3}), relative to the control device (a V_{TFL} of 0.29 V and a N_{trap} of 2.12×10^{16} cm^{-3}), representing a 38% reduction in defect states (Fig. 5e). In addition, we further evaluated the electron mobility (μ) of the perovskite films via the SCLC model (Fig. 5f), according to the following equation:

$$\mu = \frac{8L^3}{9\varepsilon_0\varepsilon_{\text{r}}}\frac{J}{V^2} \quad (5)$$

The SrI_2/IPA SSQ-treated film showcased more than 5-fold enhancement of electron mobility than that of the control film (1.32×10^{-3} cm^2 V^{-1} s^{-1} *vs.* 2.12×10^{-4} cm^2 V^{-1} s^{-1}). These improvements in defect suppression and carrier mobility are critical to achieving efficient charge transport and minimizing recombination losses, enabling high-efficiency solar-to-electricity conversion.

For real-world applications and commercialization, the universality of the post-treatment across different perovskite compositions and the yield of high-efficiency devices must be considered. The PCE histograms based on 20 devices per condition are shown in Fig. 5g. The control group exhibited lower average PCE with a broader distribution, indicating poor reproducibility. In contrast, the SrI_2/IPA SSQ-treated devices demonstrated narrower PCE distributions, with ~90% of devices falling between 19.5% to 21.0%, reflecting excellent uniformity and reproducibility. Supplementary Fig. 27 presents detailed photovoltaic parameter distributions, revealing higher and more consistent J_{SC}, FF and PCE in the quenched group. To further verify the versatility of SSQ strategy, we applied it to a variety of blade-coated WBG perovskite films. As shown in Supplementary Fig. 28 and Supplementary Table 5, the blade-coated small-area WBG devices with bandgaps of 1.65 eV ($FA_{0.8}Cs_{0.2}Pb(I_{0.85}Br_{0.15})_3$) and 1.78 eV ($FA_{0.8}Cs_{0.2}Pb(I_{0.6}Br_{0.4})_3$) achieved champion PCEs of 22.03% (J_{SC} = 22.47 mA cm^{-2}, V_{OC} = 1.20 V, FF = 81.49%) and 18.66% (J_{SC} =

17.74 mA cm^{-2}, V_{OC} = 1.29 V, FF = 81.40%), respectively. EQE measurements confirmed the bandgaps of 1.65 eV and 1.78 eV for the respective perovskite compositions (Supplementary Fig. 29). Notably, regardless of composition, the SrI_2/IPA SSQ-treated devices consistently outperformed controls in both FF and PCE, with narrower performance distributions (Supplementary Fig. 30). The method also proved effective for small-bandgap, MA-free perovskite compositions. PSCs based on SrI_2/IPA SSQ-treated $FA_{0.95}Cs_{0.05}PbI_3$ perovskite films delivered a PCE of 21.16% along with an impressive FF of 83% (Supplementary Fig. 31), validating the compositional universality of this approach.

Device operational stability was assessed under ISOS-L-1 protocols. Encapsulated devices were exposed to continuous one sun illumination at the MPP under ambient conditions (25 °C ± 5 °C, 50% ± 5% RH). As shown in Fig. 5h, control devices showed a quick PCE drop, which only retained <70% of their initial PCEs after 550 h. Encouragingly, the devices fabricated with SrI_2/IPA SSQ post-treatment maintained over 95% of their initial PCEs after 1,000 h. The time at which the PCE is projected to drop to 80% of its initial value (T_{PCE80}) is extrapolated to be 25,205 h for the target device using an appropriate linear function fitting of the experimental operational stability data in Fig. 5h (Supplementary Fig. 32)[64-66]. This substantial improvement in stability can be attributed to the synergistic effects of the solution-quenching process, which includes chemical modification, lattice reconstruction, and defect passivation. The halide salts–assisted SSQ treatment simultaneously modulated both the surface and bulk of perovskite films. Surface halide compensation and Sr^{2+} incorporation passivated defects and optimized energy-level alignment, while the rapid quenching promoted surface reconstruction and halide redistribution throughout the bulk, relieving residual stress and stabilizing the crystal lattice. These synergistic effects collectively improved device efficiency and intrinsic stability under operational conditions.

Perovskite solar modules for real-world applications

Benefiting from our successful resolution of the key challenge in achieving uniform post-treatment of large-area WBG perovskite films, we systematically evaluated the effectiveness of the SSQ strategy in enhancing WBG perovskite solar modules (PSMs). We fabricated 5.2 cm×6.0 cm WBG PSMs, and their *J-V* curves were shown in Fig. 6a. The fabrication workflow, which included all functional layer deposition and laser scribing steps, was illustrated in Supplementary Fig. 33, alongside optical microscopy image of the P1, P2 and P3 scribing channels, which enabled effective series interconnection between subcells. Each subcell was optimized to a width of 6.7 mm, and by limiting the dead-zone width to 370 μm, we achieved a high geometric FF (GFF) of ~95%. The inset in Fig. 6a shows a schematic of the four subcells connected in series, and a photo of the 5.2×6.0 cm^2 module was provided in Supplementary Fig. 34. As shown in Fig. 6a, the ~10.4 cm^2 (aperture-area) 1.68 eV WBG PSM demonstrated a PCE of 19.79% under reverse scan (J_{SC} = 4.94 mA cm^{-2}, V_{OC} = 4.98 V, FF = 80.44%) and 19.29% under forward scan (J_{SC} = 4.90 mA cm^{-2}, V_{OC} = 4.92 V, FF = 80.03%), indicating negligible hysteresis (Table 2 and Supplementary Fig. 35). The reduced hysteresis in SSQ-treated modules can be attributed to the improved quality of perovskite films with enhanced crystallinity and less defects, as well as favorable halide homogenization and stabilization, which is beneficial to suppress ion migration under operational bias. The SrI_2/IPA SSQ-treated PSMs exhibited an average PCE of 18.72% ± 0.50%, significantly outperforming both the control and the SrI_2/IPA SC-treated counterparts. Encouragingly, the 1.68 eV WBG mini-module exhibited a certified PCE of 18.42% under reverse scan, with a V_{OC} of 4.85 V, a J_{SC} of 4.89 mA cm^{-2}, and an FF of 77.72% (Supplementary Fig. 36), confirming the reliability of our reported device performance. This enhancement was also accompanied by a narrower PCE distribution, indicating improved reproducibility and consistently higher values of FF, V_{OC} and J_{SC} in the quenched group (Fig. 6b and Supplementary Fig. 37). Notably, over 69% of SSQ-treated PSMs achieved PCEs above 18.5%, compared to only 31% of the control devices demonstrated PCEs exceeding 13.5%. These results underscored the efficacy of the SSQ treatment in reliably boosting the photovoltaic performance of PSMs.

It was worth pointing out a corresponding active-area (~10.13 cm^2) efficiency of 20.32% was achieved, and the performance gap compared to the 0.04 cm^2 small-area cells (21.39% PCE) was only 1.07%, representing the smallest reported efficiency loss during upscaling of ~1.68 eV WBG perovskites using blade-coating (Supplementary Table 6). This highlighted the substantial potential of the SSQ strategy for scalable and manufacturable WBG perovskite photovoltaics. As previously mentioned, upscaling typically increases R_S, severely impacting the device FF. For example, in the control group, FF decreased from 72.00% in small-area cells to 69.95% in modules. R_S in these control PSMs reached 17.45 Ω. In contrast, after the SSQ treatment, R_S significantly dropped by 62.64% to 6.52 Ω, enabling the modules to achieve an FF as high as 80.44%, comparable to that of the small-area devices (FF = 81.26%). A systematic analysis and modeling of the relationship between R_S and FF in WBG PSMs revealed that SSQ-treated devices markedly deviated from the expected linear trend, exhibiting a greater FF enhancement than predicted for a given decrease in R_S (Supplementary Fig. 38). This improvement is attributed to a combined reduction in interfacial resistance at the perovskite/charge transport layer interfaces and the intrinsic bulk resistance of the perovskite film.

Thermal stability tests were conducted under the ISOS-D-2I protocol in an inert N_2 atmosphere at 65 °C ± 5 °C with encapsulation. As shown in Fig. 6c, the MA-free WBG PSMs treated with SrI_2/IPA SSQ retained 87% of their initial PCEs after 550 h, compared to only 43% PCE retention for the control group, confirming their strong potential for outdoor deployment. Overall, the SrI_2/IPA SSQ strategy enabled comprehensive optimization of both the bulk and surface properties of WBG perovskite films. By stabilizing halide ions, homogenizing the film surface, suppressing lattice distortion, passivating crystallographic imperfections, and improving carrier kinetics, this method significantly enhanced device efficiency, light/moisture/thermal stability, and reproducibility. These improvements translate to promising applications in portable charging devices, building-integrated photovoltaics (BIPV), agrivoltaics, and high-performance tandem photovoltaics.

To demonstrate real-world applicability, we designed integrated photovoltaic scenarios targeting both architectural and agricultural use. For building-integrated photovoltaics, we developed a smart, dual-mode four-terminal tandem solar window that combines a 1.78 eV WBG subcell with a 1.22 eV narrow-bandgap (NBG) subcell, capable of dynamically switching between transparent and opaque modes (Fig. 6d). This system adapted to varying lighting needs: under illumination-demanding conditions (translucent mode), the semi-transparent 1.78 eV WBG single-junction device operated independently, achieving a PCE of 17.22% while maintaining visible light transmittance. When shading was preferred (energy harvesting mode), the device automatically switched to a four-terminal tandem configuration, enabling synergistic utilization of both visible and near-infrared spectra, and delivering a significantly higher PCE of 27.12% (Fig. 6d, Supplementary Fig. 39 and Supplementary Table 7). Notably, the NBG subcell achieved an efficiency of 23.15%, and even under filtered light from the WBG top cell, it retained a PCE of 9.90% (Fig. 6e and Supplementary Fig. 40), which is critical for efficient tandem operation. This demonstration confirmed the potential of the SSQ strategy for realizing high-performance tandem perovskite photovoltaics and established a new paradigm for adaptive photovoltaic systems that balanced indoor comfort with on-demand energy generation in building applications. In addition, we further demonstrated the suitability of the optimized WBG PSMs for powering low-energy indoor electronics. A 5.2×6.0 cm^2 (8.5 g) WBG PSM was capable of directly powering a miniature fan (Fig. 6f) or integrated to portable power bank for charging a smartphone (Fig. 6g and Supplementary Movie 1), representing practical use cases in office or outdoor environments. For agricultural applications, we fabricated a 1.68 eV WBG semi-transparent PSM modified using the SrI_2/IPA SSQ strategy (Fig. 6h). This module exhibited an AVT of 17.55%, with a high transmittance of 28% in the red and far-red spectral range (620-760 nm) that was essential for promoting photosynthesis. Moreover, it achieved a bifacial equivalent efficiency (η_{eq}) of 18.41% with a bifaciality factor of 51.15% (Supplementary Table 8, Supplementary Figs. 41 and 42). The module was also capable of powering small-scale agricultural machinery (Fig. 6i). Collectively,

these results demonstrated that the WBG PSMs developed here could effectively meet the dual demands of energy generation and optimized light conditions for plant growth in smart agricultural environments.

Discussion

In summary, we presented an industry-inspired solution soaking quenching strategy that synergistically integrates rapid cold/thermal shock, Sr^{2+} gradient doping and halide stabilization to overcome key challenges in the crystallization heterogeneity and non-uniform surface passivation of blade-coated, large-area WBG perovskite films. This approach significantly enhanced surface compositional homogeneity, improved lattice toughness, and reduced structural defects. Our >10 cm^2, 1.68 eV WBG PSMs achieved a champion efficiency of 20.32%, outperforming other state-of-the-art blade-coated WBG perovskite modules of similar bandgap. The optimized devices retained >96% of their initial PCE after 1,000 h of continuous MPP tracking and reserved 87% PCE after 550 h at 65 °C. The strategy demonstrated broad applicability across perovskites with various bandgaps, semi-transparent modules, and four-terminal tandem architectures, enabling practical deployment in portable electronics and intelligent photovoltaic glazing. By simultaneously advancing device performance and manufacturing compatibility, this work offers a scalable solution to the performance-stability-scalability trade-off in perovskite photovoltaics, paving the way toward commercial deployment and practical application of next-generation perovskite solar technologies.

Methods

Materials

ITO-coated glasses, cesium iodide (CsI, 99.998%), lead bromide ($PbBr_2$, 99.99%) and bathocuproine (BCP, 99%) were purchased from Advanced Election Technology Co.,Ltd. Lead iodide (PbI_2, 99.999%) was purchased from Alfa Aesar. Formamidinium iodide (FAI, 99.99%) and methylammonium iodide (MAI, 99.99%) were purchased from Greatcell Solar Limited (Australia).

Poly[bis(4phenyl)(2,4,6-trimethylphenyl)amine] (PTAA, 99%), lead sulfocyanide ($Pb(SCN)_2$, 99.5%), PEDOT:PSS (Clevios VP AI 4083) and C_{60} (99%) were purchased from Xi'an Polymer Light Technology Corp. [2-(9H-Carbazol-9-yl)ethyl]phosphonic acid (2-PACz) and thylenediamine dihydroiodide ($EDAI_2$, >99%) were purchased from TCI Shanghai. Strontium iodide (SrI_2, 99.99%), tin iodide (SnI_2, 99.99%), tin (II) fluoride (SnF_2, 99%), ammonium thiocyanate (NH_4SCN, 99.99%) isopropanol (IPA, 99.8%), chlorobenzene (CB, 99.8%), N,N-dimethylformamide (DMF, 99.8%) and dimethyl sulfoxide (DMSO, 99.8%) were purchased from Sigma-Aldrich. Cuprum (Cu, 99.99%) and Argent (Ag, 99.99%) were purchased from ZhongNuo Advanced Material Beijing Technology Co., Ltd. Unless stated otherwise, all materials were used as received without further purification.

Precursor preparation

Wide-bandgap $FA_{0.8}Cs_{0.2}Pb(I_{1-x}Br_x)_3$ perovskite precursor preparation: The $FA_{0.8}Cs_{0.2}Pb(I_{1-x}Br_x)_3$ (x=0.15, 0.2, 0.4) perovskite precursor solution (1.5 M) was prepared by dissolving 1.2 mmol FAI, 0.3 mmol CsI, 1.5(1-1.5x) mmol PbI_2 and 2.25x mmol $PbBr_2$ in 1 ml mixed solvent of DMF and DMSO with a volume ratio of 7: 3. Then 9.69 mg $Pb(SCN)_2$ was added into the solution as additives. The perovskite precursor solution was thoroughly mixed and aged for 2 h before using. Then the solutions were filtered through polytetrafluoroethylene (PTFE) syringe filters (0.45 μm) before use.

Small-bandgap $FA_{0.95}Cs_{0.05}PbI_3$ perovskite precursor preparation: 1.5 M $FA_{0.95}Cs_{0.05}PbI_3$ perovskite precursor were prepared by dissolving 1.35 mmol FAI, 1.65 mmol PbI_2 and 0.15 mmol CsI in 1 ml mixed solvent of DMF and DMSO with a volume ratio of 4:1. The precursor was stirred over 2 h and then filtered by using a 0.45 μm PTFE syringe filters before use.

Narrow-bandgap Sn-Pb perovskite precursor preparation: 46.8 mg CsI, 414.9 mg PbI_2, 14.1 mg SnF_2, 85.8 mg MAI, 185.7 mg FAI, 335.3 mg SnI_2 and 2.7 mg NH_4SCN were dissolved in 1 mL

mixed solvent of DMF and DMSO with a volume ratio of 3:1. The precursor was stirred for 10 h at 50 °C. The solution was shaken to be dissolved in the glovebox.

Device fabrication

Fabrication of small-area PSCs: The indium-doped tin oxide (ITO) glasses substrates were ultrasonically cleaned by deionized water, IPA and acetone sequentially, and dried in oven. The substratess were then subjected to UV-ozone treatment for 15 min and transferred to a glove box for device preparation.

Fabrication of hole transport layer and WBG $FA_{0.8}Cs_{0.2}Pb(I_{1-x}Br_x)_3$ (1.65 eV, 1.68 eV, and 1.78 eV) and small-bandgap $FA_{0.95}Cs_{0.05}PbI_3$ perovskite films: For HTL layer, 50 μL of the PTAA/CB solution (5 mg mL^{-1}) was spin-coated on UV-ozone plasma-treated ITO glass substrate at 6,000 rpm for 30 s, followed by annealing at 100 °C for 10 min. After cooling down to room temperature, 50 μL of the 2-PACz/DMF solution (10 mg mL^{-1}) was spin-coated onto the ITO/PTAA substrate at 3,000 rpm for 30 s and annealed at 100 °C for 5 min to improve its wettability[67]. The perovskite precursors were blade-coated at a blade-speed of 5 mm s^{-1} with a gap of 100 μm, and 10 μL of perovskite ink was used for each coating. During blade-coating, a N_2 flow below 20 psi was applied to facilitate the solvent evaporation and perovskite crystallization. Then, the as-prepared perovskite films were transferred onto a hotplate and annealed at 105 °C, verified by an infrared thermometer (Supplementary Fig. 43). After 10 min, the perovskite film at 105 °C was immediately soaked into SrI_2/IPA solution (0.2 mg mL^{-1}) for 5 s, which was cooled to 5 °C in advance as the quenching liquid. The quenching speed was estimated to be 20 °C s^{-1}. After that, the perovskite film was tempered at 105 °C to complete the quenching treatment. Finally, 20 nm C_{60}, 7 nm BCP and 80 nm Ag were sequentially deposited on the perovskite films via thermal evaporation (Suzhou Fangsheng FS-450) to complete the devices.

Fabrication of hole transport layer and NBG $Cs_{0.1}FA_{0.6}MA_{0.3}Sn_{0.5}Pb_{0.5}I_3$ perovskite films: The PEDOT:PSS aqueous solution was spun onto the substrates at 4,000 rpm for 30 s, then annealed

at 150 °C for 20 min. The Sn-Pb alloying perovskite films were deposited via a two-step spin-coating process, namely, 1,000 rpm for 10 s and then 4,000 rpm for 40 s, respectively. 200 μL of CB was poured on the spinning substrate after reaching 4,000 rpm for 25 s. The substrates were immediately annealed at 120 °C for 10 min. The perovskite films were prepared in a glove-box filled with inert nitrogen atmosphere (O_2<0.01 ppm, H_2O<0.01 ppm) to carefully prevent Sn^{2+} oxidation. Finally, 30 nm C_{60}, 5 nm BCP and 150 nm Cu electrode were sequentially deposited via thermal evaporation. For the completed PSCs, they were either protected in inert atmosphere or with appropriate encapsulation during testing and characterizations.

Fabrication of PSMs: The fabrication process of the PSMs was similar to that of small-area devices except for the dosage of the precursor and the laser scribing patterning process. The schematic of fabrication procedures including all deposition and scribing steps are as follows (Supplementary Fig. 33). With an aperture area of 10.4 cm^2, the module's layout was designed as monolithic interconnection of four subcells, each with a 0.67 cm width. Firstly, the ITO-coated glass was etched by laser scribing process with a 532 nm wavelength laser, yielding a P1 line width of 27 μm. The deposition of all functional layers followed the procedures used for small-area cells, but with adjusted solution quantities, namely, 500 μL for HTL deposition and 20 μL for perovskite layer blade-coating. P2 scribing was performed after the deposition of the perovskite/C_{60}/BCP layers to scribe a line width of 120 μm. After Ag deposition, P3 was performed to scribe a line width of 59 μm, achieving the geometrical fill factor (GFF) of up to 95% for the modules, exhibiting an active-area of 10.13 cm^2.

Characterization

Steady-state and temperature-dependent photoluminescence (PL) spectra were obtained by FLS1000 (Edinburgh Instruments Ltd.), equipped with a Xe lamp, a liquid nitrogen cryostat (Oxford Instruments, Optis-tatDN-V), and a photomultiplier tube (PMT) detector. The excitation wavelength was 470 nm. PL mapping measurements were conducted using Morpho PG2000-PRO.

The morphological features of the samples were characterized using a field emission scanning electron microscope (SEM, Hitachi-SU8010) that executed at 2 kV. The atomic force microscopy (AFM) measurements were performed on a Scanning Probe Microscope (Bruker Dimension Fastscan, Bruker, Germany). The XRD patterns were characterized on an X-ray powder diffractometer with Cu Kα radiation of 1.5418 Å (Rigaku, Japan). Time-of-flight secondary ion mass spectroscopy (ToF-SIMS) measurements were carried out using a ToF-SIMS 5, ION-TOF GmbH. In situ PL measurements under light stress were performed using a mercury lamp light source (OLYMPUS, U-HGLGPS), which provided 130 W output in the 460-490 nm range. GIWAXS images were collected using a Xeuss 2.0 spectrometer (Xenocs company) with MetalJet-D2 (Excillum) as the X-ray source and Pilatus 3R 1M (Dectris) as the detector. Glancing incident angle X-ray diffraction (GIXRD) was performed on a D8-discover 25 diffractometer (Bruker). Valence band (VB) measurements were performed via UPS, employing a bias of 5 V and Au as a reference. Illumination intensity-dependent photoluminescence quantum yield (PLQY) measurements were conducted using the LuminQY system (Ideaoptics). The femtosecond transient absorption (fs-TA) spectroscopy was conducted by equipping a re-generatively amplified Ti: Sapphire laser source (Coherent Legend, 800 nm, 150 fs, 5 Jm pulse^{-1}, and 1 kHz repetition rate) and Helios (Ultrafast Systems LLC) spectrometers. A 75% portion of the 800 nm output pulse was frequency-doubled in a BaB_2O_4 (BBO) crystal, which could generate 400 nm pump light. Meanwhile, the remaining portion of the output was concentrated into a sapphire window to produce a white light continuum (320-780 nm) probe light. The 400 nm pump beam was generated as part of the 800 nm output pulse from the amplifier, and its power was adjusted by a range of neutral-density filters. The pump beam was focused at the sample with a beam waist of 360 μm; the power intensity was fixed at 14 μJ cm^{-2} in this experiment. With the aid of the mechanical chopper, the pump repetition frequency was synchronized to 500 Hz. The probe and reference beams could be split from the white-light continuum and sent into a fiber optics-coupled multichannel spectrometer by complementary metal oxide-semiconductor sensors with a

frequency of 1 kHz. The *J-V* characteristics and the steady photocurrent under maximum power output bias (1.05 V) of PSCs/PSMs were measured in ambient air (25 °C ± 5 °C and 40% ± 10% relative humidity) using a Keithley 2400 source-meter under simulated AM1.5G one sun illumination (100 mW cm^{-2}) generated by a solar simulator (the Oriel Sol3A Class AAA) based on Xenon lamps. The light intensity was calibrated by a silicon reference cell equipped with a SCHOTT visible color KG3 glass filter (Newport 91150V). All the devices were tested using non-reflective shadow masks with an aperture area of 0.04 cm^2 for the small-area devices and 10.4 cm^2 for the large-area PSMs, respectively. The *J-V* curves were measured from 1.4 V to -0.1 V or from -0.1 V to 1.4 V for the small-area devices, and from 5.5 V to -0.1 V or from -0.1 V to 5.5 V for the large-area PSMs with a scan rate of 0.1 V s^{-1}. For the space charge limited current (SCLC) test, the *J–V* characteristics were measured using a CH Instruments CHI660 electrochemical workstation (ChenHua, China) in a shield box with a structure of ITO/SnO_2/perovskite/C_{60}/BCP/Cu. External quantum efficiency (EQE) was measured with the solar cell quantum efficiency measurement system (SCS10, Zolix Instruments Co., Ltd., China) at wavelength regions from 300 nm to 850 nm. The optical photo of scribing for subcell separation in modules were conducted by optical microscope (Olympus BX53MRF-S).

Light stability test: The devices used for operational stability test were encapsulated by cover glass with edges sealed by butyl tape. The long-term MPP tracking of the encapsulated devices was carried out on Multi-Channels Solar Cells Stability Test System (Wuhan 91PVKSolar Technology Co. Ltd, China) in ambient air with a relative humidity of 50% ± 5%, following the protocol (ISOS-L-1). The digital source meter (Keithley 2400) was used to record the current density-voltage (*J–V*) data under AM 1.5G one sun illumination (100 mW cm^2).

Thermal stability test: The devices were placed on a heating stage at 65 °C ± 5 °C in a N_2 glove box with encapsulation, following the ISOS-D-2I protocol. The thermal stability assessments were carried out by repeating the *J-V* characterizations upon heating the devices for different duration.

Statistical analysis

All statistical analysis was performed with Origin 2021. For TA data normalization, the maximum values of the dynamic TA decay lifetime were normalized to 1. To investigate the PCE statistical distribution of small-area PSCs, the histograms of 20 solar cells were used to generate the device performance statistics (Fig. 5g) and calculate the average PCEs with standard deviation (Table 1). To investigate the PCE statistical distribution of large-area PSMs, the histograms of 16 solar modules were used to generate the device performance statistics (Fig. 6b) and calculate the average PCEs with standard deviation (Table 2).

Competing interests: The authors declare that they have no competing interests.

Data availability

All data generated in this study are provided in the main text and Supplementary Information or upon request from the corresponding author.

References

1 Wang, Y. *et al.* Homogenized contact in all-perovskite tandems using tailored 2D perovskite. *Nature* **635**, 867-873 (2024).

2 National Renewable Energy Laboratory (NREL). Photovoltaic Research, Best Research-Cell Efficiency Chart. <https://www.nrel.gov/pv/cell-efficiency.html> (2026).

3 Yang, M. *et al.* Chemical synergic stabilization of high Br-content mixed-halide wide-bandgap perovskites for durable multi-terminal tandem solar cells with minimized Pb leakage. *Angew. Chem. Int. Ed.* **64**, e202415966 (2025).

4 Wang, Z. *et al.* Regulation of wide bandgap perovskite by rubidium thiocyanate for efficient silicon/perovskite tandem solar cells. *Adv. Mater.* **36**, 2407681 (2024).

5 Kang, S. *et al.* Boosting carrier transport in quasi-2D/3D perovskite heterojunction for high-performance perovskite/organic tandems. *Adv. Mater.* **37**, 2411027 (2025).

6 Scheler, F. *et al.* Correlation of band bending and ionic losses in 1.68 eV wide band gap perovskite solar cells. *Adv. Energy Mater.* **15**, 2404726 (2024).

7 Wąsiak-Maciejak, A. *et al.* Compositional and interfacial engineering for improved light stability of flexible wide-bandgap perovskite solar cells. *J. Mater. Chem. A* **13**, 7335-7346 (2025).

8 Feng, W. *et al.* Blade-coating (100)-oriented α-$FAPbI_3$ perovskite films via crystal surface energy regulation for efficient and stable inverted perovskite photovoltaics. *Angew. Chem. Int. Ed.* **63**, e202403196 (2024).

9 Duan, C. *et al.* Scalable fabrication of wide-bandgap perovskites using green solvents for tandem solar cells. *Nat. Energy* **10**, 318-328 (2025).

10 Zhao, X. *et al.* Operationally stable perovskite solar modules enabled by vapor-phase fluoride treatment. *Science* **385**, 433-438 (2024).

11 Deng, Y. *et al.* Surfactant-controlled ink drying enables high-speed deposition of perovskite films for efficient photovoltaic modules. *Nat. Energy* **3**, 560-566 (2018).

12 Huang, C. *et al.* Meniscus-modulated blade coating enables high-quality α-phase formamidinium lead triiodide crystals and efficient perovskite minimodules. *Joule* **8**, 2539-2553 (2024).

13 Liu, Q. *et al.* Enhancing the efficiency and stability of inverted perovskite solar cells and modules through top interface modification with n-type semiconductors. *Angew. Chem. Int. Ed.* **64**, e202416390 (2025).

14 Wang, H. *et al.* Impurity-healing interface engineering for efficient perovskite submodules. *Nature* **634**, 1091-1095 (2024).

15 Zhou, H. *et al.* Efficient and stable perovskite mini-module via high-quality homogeneous perovskite crystallization and improved interconnect. *Nat. Commun.* **15**, 6679 (2024).

16 Zhou, S. *et al.* Aspartate all-in-one doping strategy enables efficient all-perovskite tandems. *Nature* **624**, 69-73 (2023).

17 Zai, H. *et al.* Wafer-scale monolayer MoS_2 film integration for stable, efficient perovskite solar cells. *Science* **387**, 186-192 (2025).

18 Azam, M. *et al.* Tailoring pyridine bridged chalcogen-concave molecules for defects passivation enables efficient and stable perovskite solar cells. *Nat. Commun.* **16**, 602 (2025).

19 Liu, Z. *et al.* Reducing perovskite/C_{60} interface losses via sequential interface engineering for efficient perovskite/silicon tandem solar cell. *Adv. Mater.* **36**, 2308370 (2024).

20 Jiang, X. *et al.* Isomeric diammonium passivation for perovskite–organic tandem solar cells. *Nature* **635**, 860-866 (2024).

21 Wang, C. *et al.* A wenzel interfaces design for homogeneous solute distribution obtains efficient and stable perovskite solar cells. *Adv. Mater.* **37**, 2417779 (2025).

22 Yunker, P. J., Still, T., Lohr, M. A. & Yodh, A. G. Suppression of the coffee-ring effect by shape-dependent capillary interactions. *Nature* **476**, 308-311 (2011).

23 Liao, X. *et al.* Methylammonium-free, high-efficiency, and stable all-perovskite tandem solar cells enabled by multifunctional rubidium acetate. *Nat. Commun.* **16**, 1164 (2025).

24 Turren-Cruz, S.-H., Hagfeldt, A. & Saliba, M. Methylammonium-free, high-performance, and stable perovskite solar cells on a planar architecture. *Science* **362**, 449-453 (2018).

25 Fakharuddin, A. *et al.* Inorganic and layered perovskites for optoelectronic devices. *Adv. Mater.* **31**, 1807095 (2019).

26 Sha, H. *et al.* Probing carrier trapping and hysteresis at perovskite grain boundaries via in situ characterization. *Opt. Mater.* **139**, 113817 (2023).

27 Ye, C. *et al.* Activating metal oxides nanocatalysts for electrocatalytic water oxidation by quenching-induced near-surface metal atom functionality. *J. Am. Chem. Soc.* **143**, 14169-14177 (2021).

28 Dong, Q. *et al.* Programmable heating and quenching for efficient thermochemical synthesis. *Nature* **605**, 470-476 (2022).

29 Mei, J. & Yan, F. Recent advances in wide-bandgap perovskite solar cells. *Adv. Mater.* **37**, 2418622 (2025).

30 Kim, K., Moon, T. & Kim, J. Wide Bandgap Perovskites: A Comprehensive Review of Recent Developments and Innovations. *Small* **21**, 2407007 (2025).

31 Li, N. *et al.* Liquid medium annealing for fabricating durable perovskite solar cells with improved reproducibility. *Science* **373**, 561-567 (2021).

32 Li, J. *et al.* Accelerating thermal transfer in perovskite films for high-efficiency and stable photovoltaics. *Adv. Funct. Mater.* **33**, 2308036 (2023).

33 Zheng, Y. *et al.* Downward homogenized crystallization for inverted wide-bandgap mixed-halide perovskite solar cells with 21% efficiency and suppressed photo-induced halide segregation. *Adv. Funct. Mater.* **32**, 2200431 (2022).

34 Datta, K. *et al.* Local halide heterogeneity drives surface wrinkling in mixed-halide wide-bandgap perovskites. *Nat. Commun.* **16**, 1967 (2025).

35 Hoke, E. T. *et al.* Reversible photo-induced trap formation in mixed-halide hybrid perovskites for photovoltaics. *Chem. Sci.* **6**, 613-617 (2015).

36 Nie, T. *et al.* Advances in single-halogen wide-bandgap perovskite solar cells. *Adv. Funct. Mater.* **35**, 2416264 (2025).

37 Leijtens, T., Bush, K. A., Prasanna, R. & McGehee, M. D. Opportunities and challenges for tandem solar cells using metal halide perovskite semiconductors. *Nat. Energy* **3**, 828-838 (2018).

38 Belisle, R. A. *et al.* Impact of surfaces on photoinduced halide segregation in mixed-halide perovskites. *ACS Energy Lett.* **3**, 2694-2700 (2018).

39 Wu, W.-Q. *et al.* Reducing surface halide deficiency for efficient and stable iodide-based perovskite solar cells. *J. Am. Chem. Soc.* **142**, 3989-3996 (2020).

40 Lu, Y.-N. *et al.* Constructing an n/n^+ homojunction in a monolithic perovskite film for boosting charge collection in inverted perovskite photovoltaics. *Energy Environ. Sci.* **14**, 4048-4058 (2021).

41 Saidaminov, M. I. *et al.* Suppression of atomic vacancies via incorporation of isovalent small ions to increase the stability of halide perovskite solar cells in ambient air. *Nat. Energy* **3**, 648-654 (2018).

42 Shai, X. *et al.* Efficient planar perovskite solar cells using halide Sr-substituted Pb perovskite. *Nano Energy* **36**, 213-222 (2017).

43 Zhao, Y. *et al.* Divalent hard Lewis acid doped $CsPbBr_3$ films for 9.63%-efficiency and ultra-stable all-inorganic perovskite solar cells. *J. Mater. Chem. A* **7**, 6877-6882 (2019).

44 Li, N. *et al.* Efficient and stable $FA_{0.95}Cs_{0.05}PbI_3$ single-crystal perovskite solar cells via hierarchical elimination of surface iodide vacancies. *ACS Nano* **19**, 42826-42834 (2025).

45 Simbula, A. *et al.* Exciton dissociation in 2D layered metal-halide perovskites. *Nat. Commun.* **14**, 4125 (2023).

46 Huang, T. *et al.* Performance-limiting formation dynamics in mixed-halide perovskites. *Sci. Adv.* **7**, eabj1799 (2021).

47 Chen, Y. *et al.* Nuclei engineering for even halide distribution in stable perovskite/silicon tandem solar cells. *Science* **385**, 554-560 (2024).

48 Qin, M., Chan, P. F. & Lu, X. A systematic review of metal halide perovskite crystallization and film formation mechanism unveiled by in situ GIWAXS. *Adv. Mater.* **33**, 2105290 (2021).

49 Zhou, Q., Duan, J., Yang, X., Duan, Y. & Tang, Q. Interfacial strain release from the WS_2/$CsPbBr_3$ van der waals heterostructure for 1.7 V voltage all-inorganic perovskite solar cells. *Angew. Chem. Int. Ed.* **59**, 21997-22001 (2020).

50 Wang, Y. *et al.* Lattice mismatch at the heterojunction of perovskite solar cells. *Angew. Chem. Int. Ed.* **63**, e202405878 (2024).

51 Chang, X. *et al.* Two-second-annealed 2D/3D perovskite films with graded energy funnels and toughened heterointerfaces for efficient and durable solar cells. *Angew. Chem. Int. Ed.* **135**, e202309292 (2023).

52 Wang, H. *et al.* Interfacial residual stress relaxation in perovskite solar cells with improved stability. *Adv. Mater.* **31**, 1904408 (2019).

53 Muscarella, L. A. & Ehrler, B. The influence of strain on phase stability in mixed-halide perovskites. *Joule* **6**, 2016-2031 (2022).

54 Wu, L. *et al.* Resilience pathways for halide perovskite photovoltaics under temperature cycling. *Nat. Rev. Mater.* **10**, 536–549 (2025).

55 Li, L. *et al.* In-Situ polymer framework strategy enabling printable and efficient perovskite solar cells by mitigating "coffee ring" effect. *Adv. Mater.* **36**, 2310752 (2024).

56 Ramirez, C., Yadavalli, S. K., Garces, H. F., Zhou, Y. & Padture, N. P. Thermo-mechanical behavior of organic-inorganic halide perovskites for solar cells. *Scr. Mater.* **150**, 36-41 (2018).

57 Liu, G. *et al.* Synergic electron and defect compensation minimizes voltage loss in lead-free perovskite solar cells. *Angew. Chem. Int. Ed.* **62**, e202305551 (2023).

58 Zhang, X. *et al.* Heterostructural $CsPbX_3$-PbS (X = Cl, Br, I) quantum dots with tunable Vis–NIR dual emission. *J. Am. Chem. Soc.* **142**, 4464-4471 (2020).

59 Zhu, Z. *et al.* Efficiency enhancement of perovskite solar cells through fast electron extraction: The role of graphene quantum dots. *J. Am. Chem. Soc.* **136**, 3760-3763 (2014).

60 Hadke, S. *et al.* Suppressed deep traps and bandgap fluctuations in Cu_2CdSnS_4 solar cells with ≈8% efficiency. *Adv. Energy Mater.* **9**, 1902509 (2019).

61 Park, J. *et al.* Controlled growth of perovskite layers with volatile alkylammonium chlorides. *Nature* **616**, 724-730 (2023).

62 Liu, N. *et al.* Particle decoration enables solution-processed perovskite integration with fully-textured silicon for efficient tandem solar cells. *Nat. Commun.* **16**, 9435 (2025).

63 Stolterfoht, M. *et al.* How to quantify the efficiency potential of neat perovskite films: Perovskite semiconductors with an implied efficiency exceeding 28%. *Adv. Mater.* **32**, 2000080 (2020).

64 Nie, R. *et al.* Enhanced coordination interaction with multi-site binding ligands for efficient and stable perovskite solar cells. *Nat. Commun.* **16**, 6438 (2025).

65 Mo, K. *et al.* Minimizing DMSO residues in perovskite films for efficient and long-term stable solar cells. *Adv. Energy Mater.* **15**, 2404538 (2025).

66 Dong, Z. *et al.* Intermediate phase evolution for stable and oriented evaporated wide-bandgap perovskite solar cells. *Nat. Mater.* (2025), DOI: 10.1038/s41563-025-02375-8.

67 Tan, Y. *et al.* Chemical linkage and passivation at buried interface for thermally stable inverted perovskite solar cells with efficiency over 22%. *CCS Chemistry* **5**, 1-13 (2022).

Acknowledgments

This work was financially supported by the National Key R&D Program of China (grant number 2025YFE0106500 to W.-Q.W.), Guangzhou Science and Technology Programme (grant number 2024B03J1227 to W.-Q.W.), the Guangdong Basic and Applied Basic Research Foundation (grant number 2023B1515120008, 2024A1515011571 to W.-Q.W.), and the National Natural Science Foundation of China (grant number 52472115 to W.-Q.W.).

Author contributions

W.-Q.W. and Y.F. conceived and designed the research. Y.F. carried out the fabrication and characterization of WBG PSCs and PSMs. J.S. and Y.T. helped to optimize WBG PSCs and PSMs. G.Y. carried out the fabrication and characterization of NBG PSCs and TSCs. Y.F. and H.C. carried out PL Steady-state and temperature-dependent steady-state PL measurements and data analysis. M.G. helped to optimize the semitransparent WBG PSM. Y.F., M.Y. and Y.Feng carried out SEM and AFM measurements and data analysis. H. L. carried out GIWAXS measurement and data

analysis. J.F. carried out GIXRD measurement and data analysis. C.W., L.Q., J.G., Z.Y. helped with experimental design and data analysis. Y. F. and W.-Q. W. completed the writing of the manuscript. W.-Q. W. directed and supervised this project. All authors discussed the results and commented on the manuscript.

Competing interests

The authors declare that they have no competing interests.

Tables

Table 1. Summarized photovoltaic parameters of the control and SrI_2/IPA SSQ-treated 1.68 eV WBG PSCs under AM 1.5G one sun illumination (100 mW cm^{-2}).

Devices		V_{OC} (V)	J_{SC} (mA cm^{-2})	FF (%)	PCE (%)	Average PCE (%)
control	reverse	1.18	19.90	72.00	16.91	14.97 ± 0.84
	forward	1.18	19.31	72.00	16.41	
SrI_2/IPA SSQ	reverse	1.21	21.68	81.26	21.39	20.28 ± 0.54
	forward	1.20	21.46	81.30	20.94	

Note: the average PCE was determined by a batch of 20 devices for each condition.

Table 2. Summarized photovoltaic parameters of the PSMs (aperture area of 10.4 cm^2, four subcells in series) without or with SrI_2/IPA SSQ post-treatment measured under AM 1.5G one-sun illumination (100 mW cm^{-2}).

PSMs		V_{OC} (V)	J_{SC} (mA cm^{-2})	FF (%)	PCE (%)	R_S (Ω)
control	reverse	4.42	4.53	69.95	14.03	17.45
	forward	4.42	4.50	68.56	13.64	
	average[a)]	4.51±0.15	4.53±0.13	64.94±3.93	13.52±0.64	22.67±4.97

SrI_2/IPA SC	reverse	4.94	4.77	70.72	16.65	13.61
	forward	4.71	4.80	68.78	15.56	
	average[a)]	4.61±0.16	4.60±0.09	71.9±62.59	15.27±0.79	11.67±1.44
SrI_2/IPA SSQ	reverse	4.98	4.94	80.44	19.78	6.52
	forward	4.92	4.90	80.03	19.30	
	average[a)]	4.92±0.03	4.78±0.11	79.70±0.52	18.72 ±0.50	6.98±0.20

[a)] The average PCE was determined across four batches of 16 modules for each condition.

Figure Captions

Fig. 1: SSQ post-treatment and chemical homogeneity of large-scale WBG perovskite films. **a** Schematic illustration of solution soaking quenching of perovskite film. Inset shows the industrial metallurgical quenching approach. SEM images of the WBG perovskite films **b** w/o and **c** with SrI_2/IPA SSQ treatment, respectively. Scale bar, 500 nm. **d** Blade-coated, large-area (5.2 cm × 6.0 cm) perovskite film divided into 13 distinct regions. **e** Normalized PL intensity of different locations of large-area WBG perovskite films. **f** Bright-field microscopy and confocal PL mappings of the **g** control, **h** SrI_2/IPA SC- and **i** SrI_2/IPA SSQ-treated perovskite films across 13 designated regions. Scale bar, 200 μm in **f**.

Fig. 2: SSQ-assisted crystallization modulation for halide stabilization and thermal stability enhancement. **a** Schematic diagram of crystallization and film formation of blade-coated perovskite precursor. **b** Phase segregation induced by halide ion migration through halide vacancy pathway under light exposure or thermal stress. **c** Schematic of the Sr^{2+} penetration, passivation and stabilization mechanisms upon SrI_2/IPA SC or SSQ treatment. ToF-SIMS depth-profile analysis of the **d** SrI_2/IPA SC and **e** SrI_2/IPA SSQ-treated mixed-halide WBG perovskite films.

Color plots of normalized PL spectra for the **f** control, **g** SrI_2/IPA SC and **h** SrI_2/IPA SSQ-treated mixed-halide WBG perovskite films measured at increasing temperatures from 100 K to 320 K.

Fig. 3: SSQ-assisted surface reconstruction and lattice strain modulation. GIWAXS patterns of the **a-c** control, **d-f** SrI_2/IPA SC-treated and **g-i** SrI_2/IPA SSQ-treated WBG perovskite films measured with different incidence angles from 1° to 2°. GIXRD patterns measured at different Ψ angles from 5° to 45° for the **j** control, **k** SrI_2/IPA SC-treated and **l** SrI_2/IPA SSQ-treated WBG perovskite films. **m** 2θ versus $\sin^2\Psi$ plots for the control, SrI_2/IPA SC-treated and SrI_2/IPA SSQ-treated WBG perovskite films. **n** Schematic of the tensile stress release via SrI_2/IPA SC and SSQ post-treatment. Note, δ_R is the calculated residual stress.

Fig. 4: SSQ-assisted energy level alignment and carrier dynamics optimization. a Energy level alignments between different perovskite films and adjacent functional layers. Note, E_{vac} is the vacuum level, E_F is the Fermi level, CB and VB are the conduction band and valence band, respectively. **b** Schematic illustration of the device architecture for TA measurement. The contour plots and delay time-dependent TA spectra of the stacked semi-devices based on the **c, e** control and **d, f** SrI_2/IPA SSQ-treated WBG perovskite films, where a 400 nm pump pulse was generated by a fs-laser. **g** Dynamic TA decay lifetime probed at the GSB peak for the semi-devices based on the control and SrI_2/IPA SSQ-treated WBG perovskite films.

Fig. 5: Photovoltaic performance and stability of different WBG PSCs. a Schematic illustration of the inverted *p-i-n* PSC. **b** *J-V* curves of the 1.68 eV WBG PSCs fabricated without (control) or with SrI_2/IPA SSQ post-treatment measured under reverse or forward scanning directions. **c** Stabilized current density and PCE of the champion SrI_2/IPA SSQ-treated PSC operated at the maximum power point of 1.05 V. **d** EQE spectra and integrated J_{SC} values of the PSCs without or with SrI_2/IPA SSQ post-treatment. **e** SCLC curves and **f** calculated electron

mobility of the electron-only devices based on the WBG perovskite films without or with SrI_2/IPA SSQ post-treatment. **g** PCE histograms of the control and SrI_2/IPA SSQ-treated WBG PSCs (active-area: 0.04 cm^2) from 20 devices for each condition. **h** MPP tracking of the encapsulated control and SrI_2/IPA SSQ-treated WBG PSCs under continuous one sun illumination in ambient environment following the ISOS-L-1 protocol.

Fig. 6: Large-scale WBG PSMs and multi-scenario applications. a The *J-V* curves of the best-performing control, SrI_2/IPA SC-treated, SrI_2/IPA SSQ-treated 1.68 eV WBG PSMs with an aperture area of 10.4 cm^2. The inset shows the schematic of a four-subcell series-connected module. **b** PCE histograms of the control, SrI_2/IPA SC-treated, SrI_2/IPA SSQ-treated 1.68 eV WBG PSMs from 16 devices for each condition (12 independent batches). **c** PCE tracking of the encapsulated control and SrI_2/IPA SSQ-treated WBG PSMs heated at 65 °C in an inert N_2 atmosphere following the ISOS-D-2I protocol. **d** Schematic of the smart photovoltaic window that could be switchable between translucent mode (single-junction semitransparent WBG PSC) and energy harvesting mode (opaque tandem PSC). **e** *J-V* curves of 1.22 eV NBG PSC, filtered 1.22 eV NBG PSC, and semi-transparent 1.78 eV WBG PSC. The photographs of WBG PSM-powered **f** desktop mini fan and **g** the portable power bank. **h** The photograph of the semitransparent WBG PSM integrated for agrivoltaics. **i** The photograph of the WBG PSM-powered tool car under sunlight on clear days.

Editor's Summary

Fang et al. report a scalable solution-soaking quenching technique to enable uniform passivation of large-area wide-bandgap perovskite films, resulting in 10.13-cm2 solar modules with 20.32% efficiency, prolonged lifespan, and applications in tandem solar windows, transparent agrivoltaics, and portable power systems.

Peer review information: *Nature Communications* thanks Mingkui Wang, Hong Zhang and the other anonymous reviewer(s) for their contribution to the peer review of this work. A peer review file is available.

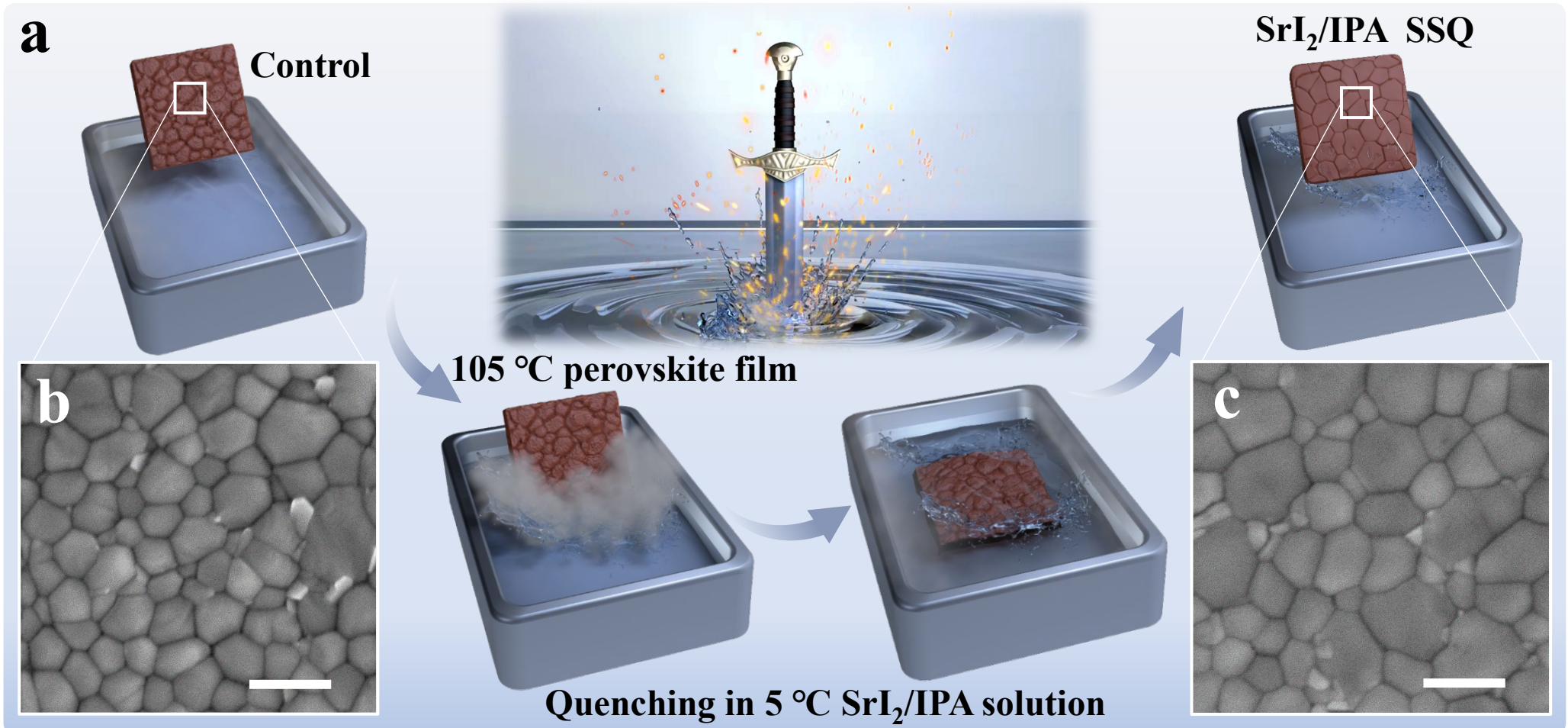
a
Control
SrI2/IPA SSQ
105 ℃ perovskite film
Quenching in 5 ℃ SrI2/IPA solution
b
c

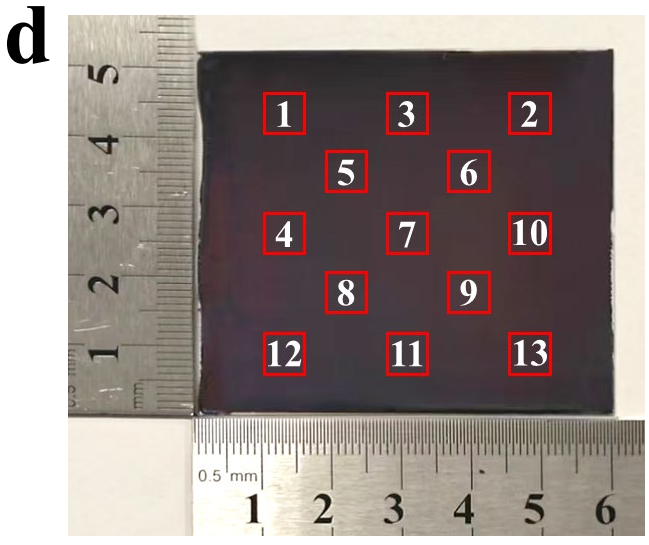
d
1
3
2
5
6
4
7
10
8
9
12
11
13
0.5 mm

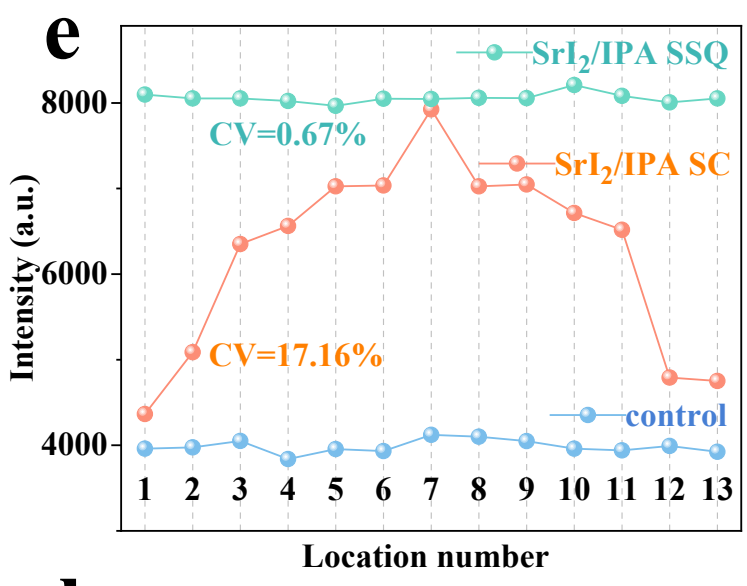
e
SrI2/IPA SSQ
SrI2/IPA SC
control
CV=0.67%
CV=17.16%
Intensity (a.u.)
8000
6000
4000
1 2 3 4 5 6 7 8 9 10 11 12 13
Location number

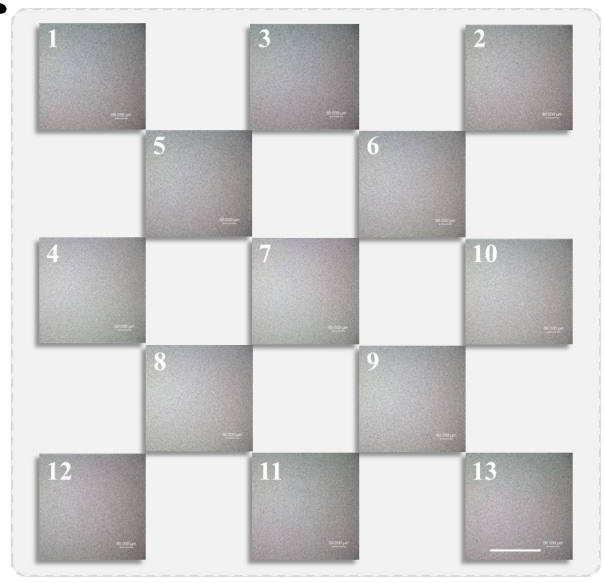
f
1
3
2
5
6
4
7
10
8
9
12
11
13

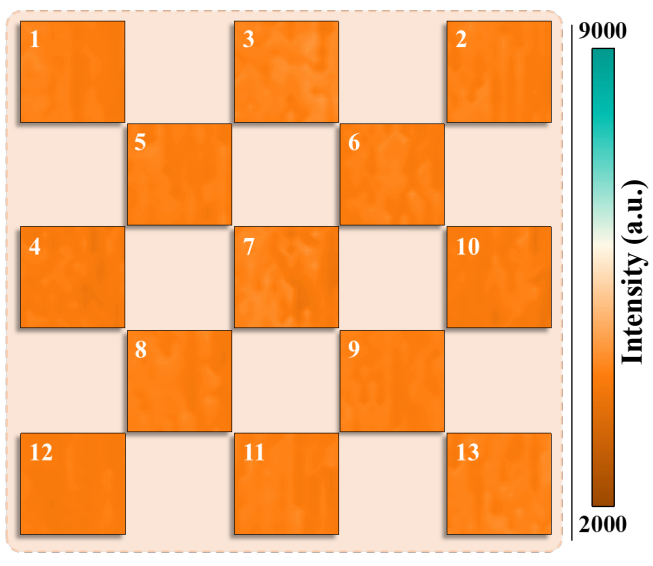
g
1
3
2
5
6
4
7
10
8
9
12
11
13
9000
2000
Intensity (a.u.)

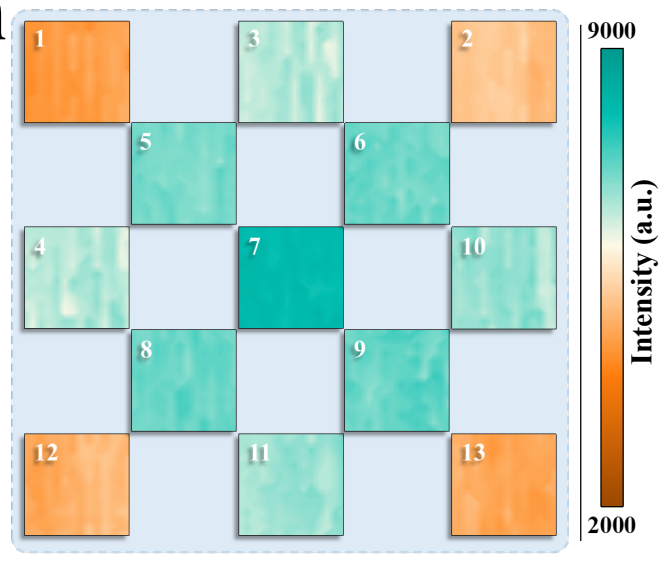
h
1
3
2
5
6
4
7
10
8
9
12
11
13
9000
2000
Intensity (a.u.)

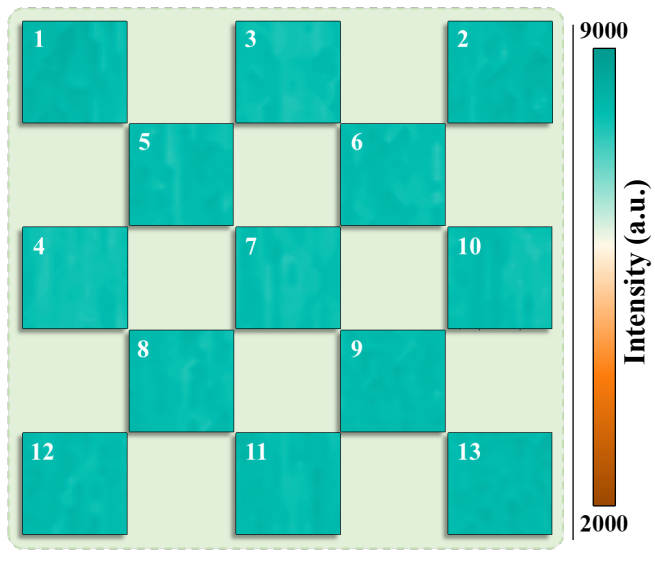
i
1
3
2
5
6
4
7
10
8
9
12
11
13
9000
2000
Intensity (a.u.)

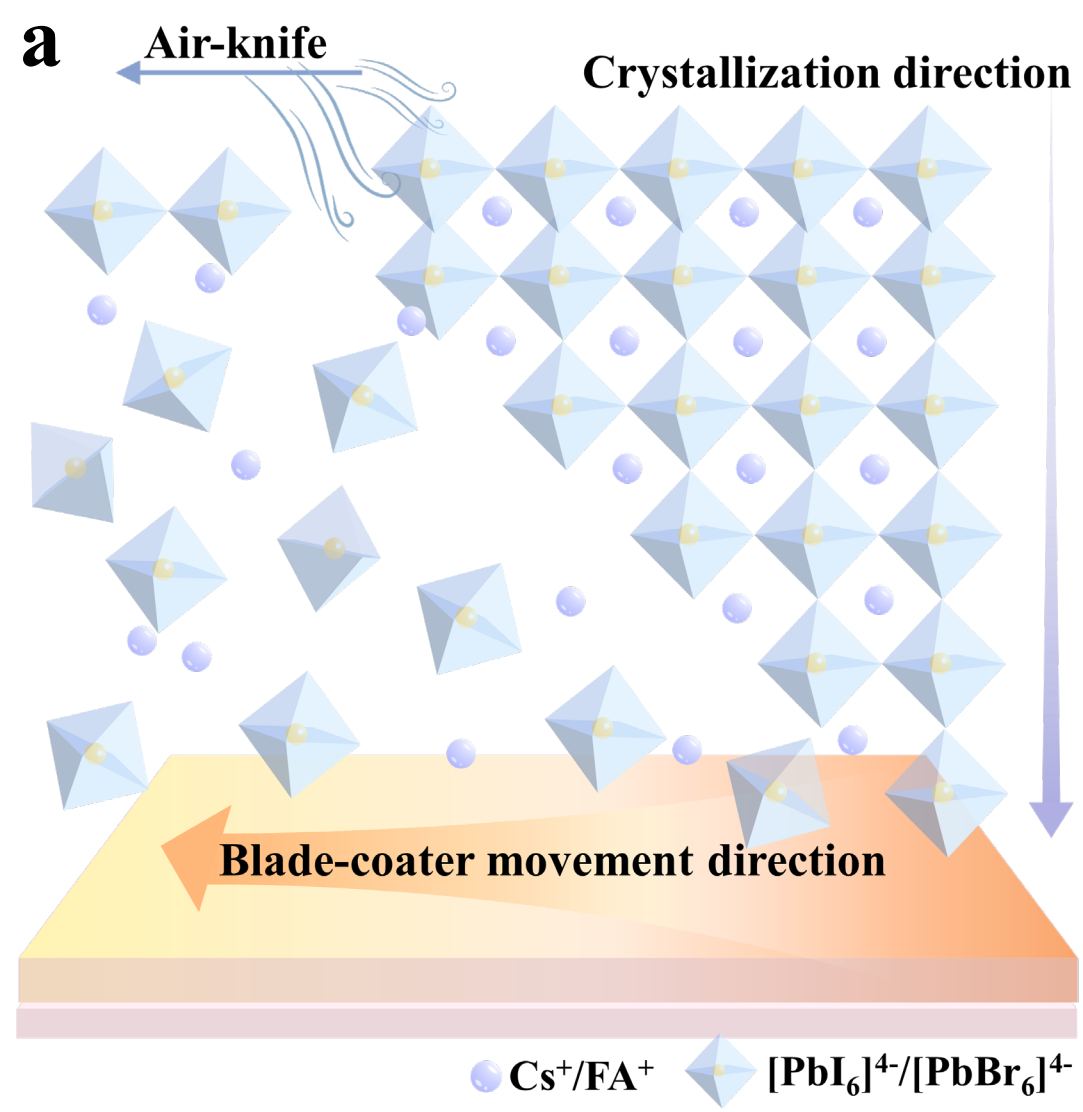
a
Air-knife
Crystallization direction
Blade-coater movement direction
Cs+/FA+
[PbI6]4-/[PbBr6]4-

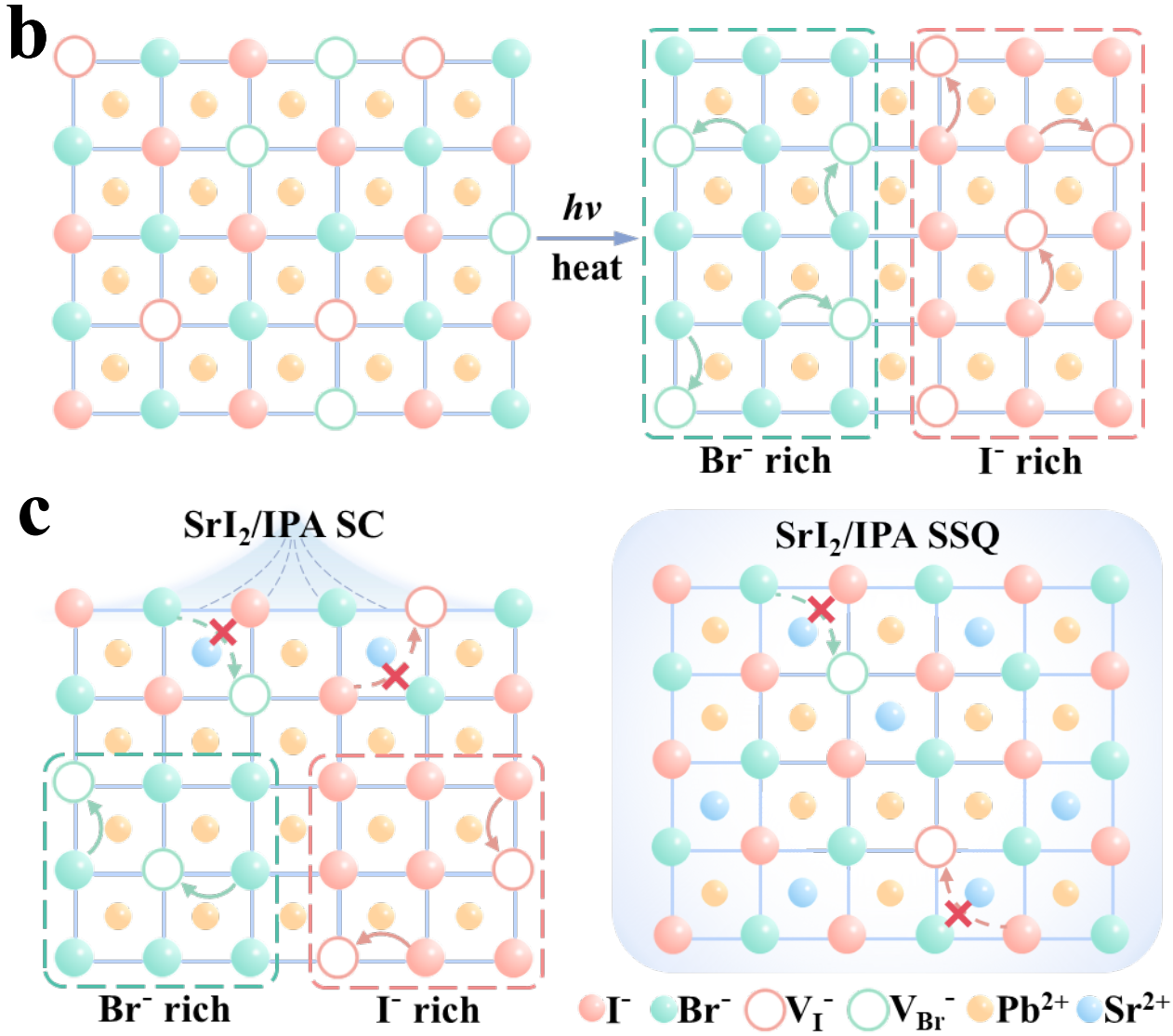
b
hv
heat
Br- rich
I- rich
c
SrI2/IPA SC
SrI2/IPA SSQ
Br- rich
I- rich
I-
Br-
VI-
VBr-
Pb2+
Sr2+

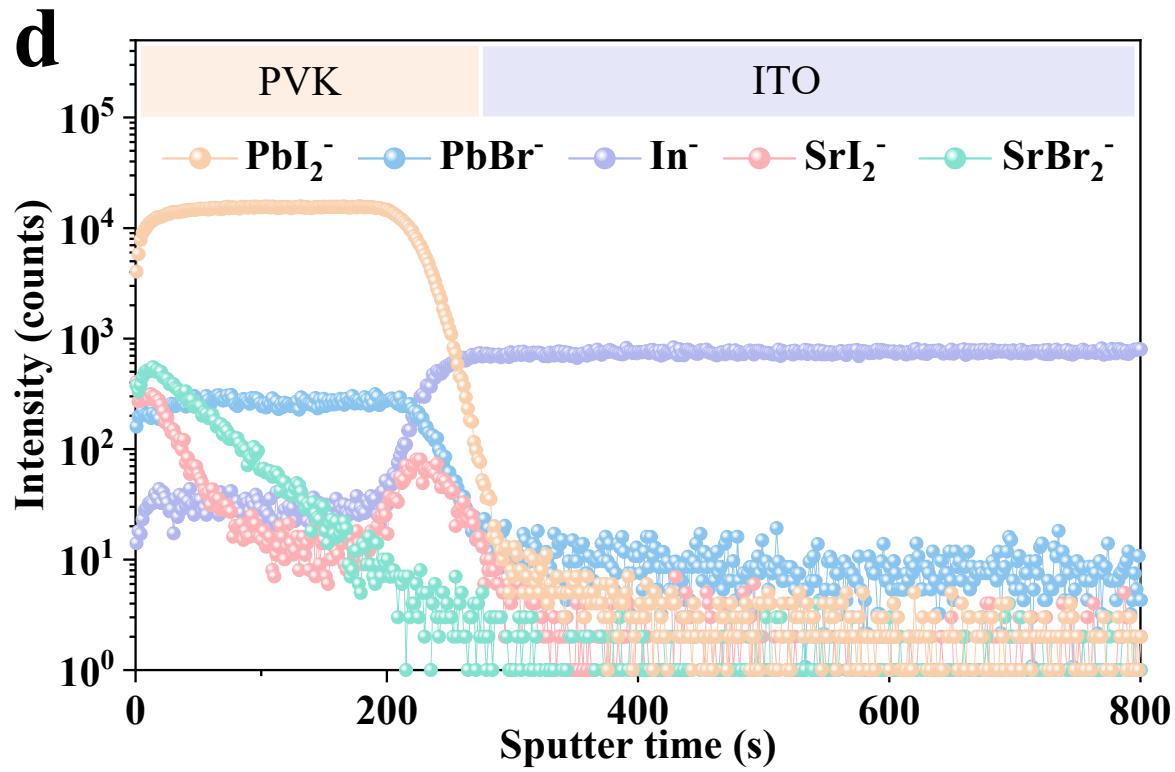
d
PVK
ITO
PbI2-
PbBr-
In-
SrI2-
SrBr2-
Intensity (counts)
Sputter time (s)

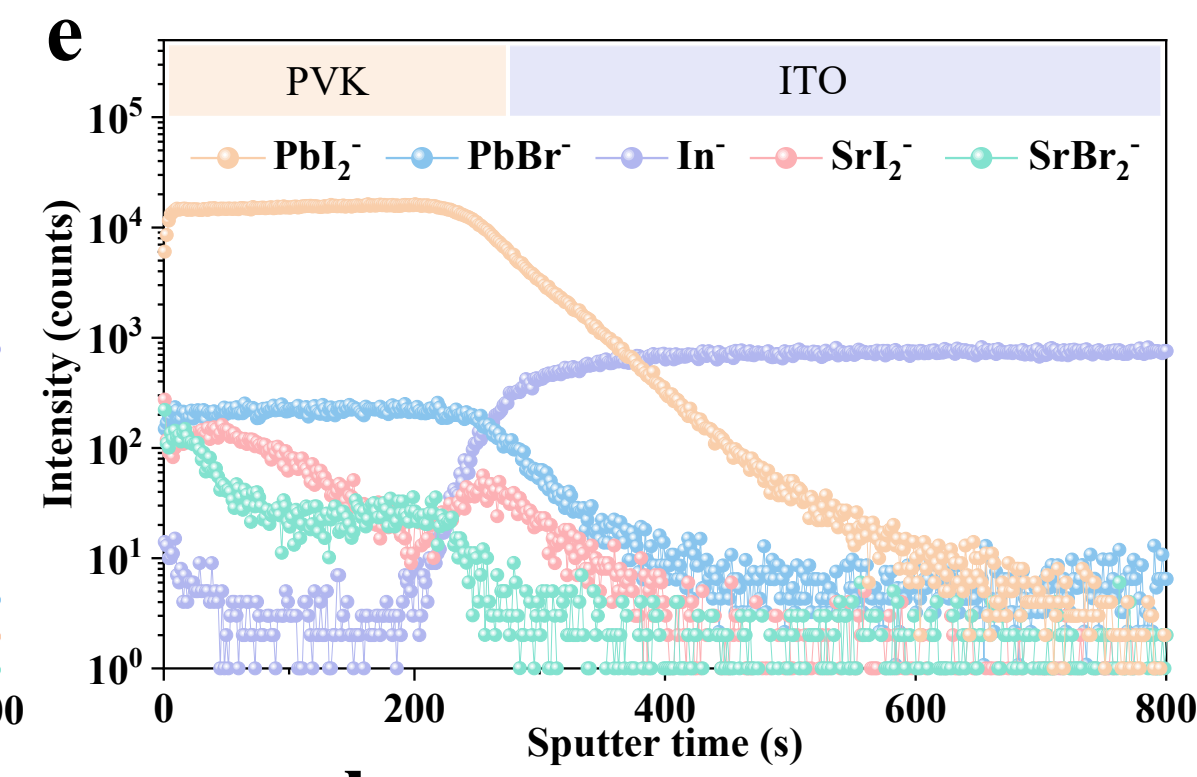
e
PVK
ITO
PbI2-
PbBr-
In-
SrI2-
SrBr2-
Intensity (counts)
Sputter time (s)

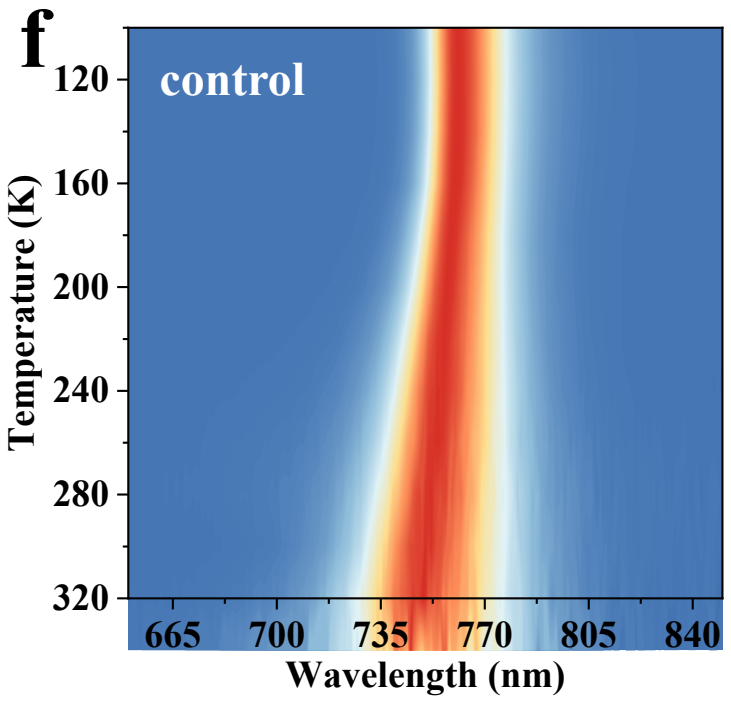
f
control
Temperature (K)
Wavelength (nm)

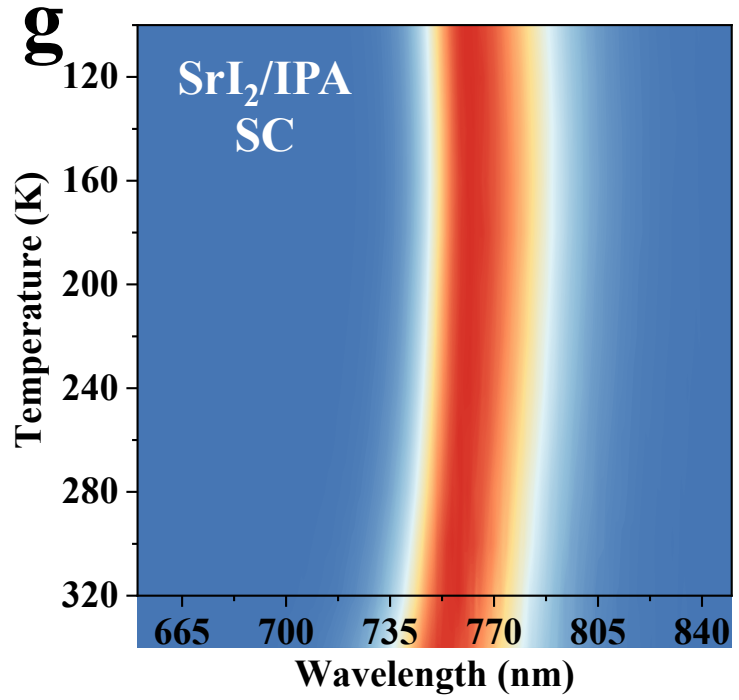
g
SrI2/IPA SC
Temperature (K)
Wavelength (nm)

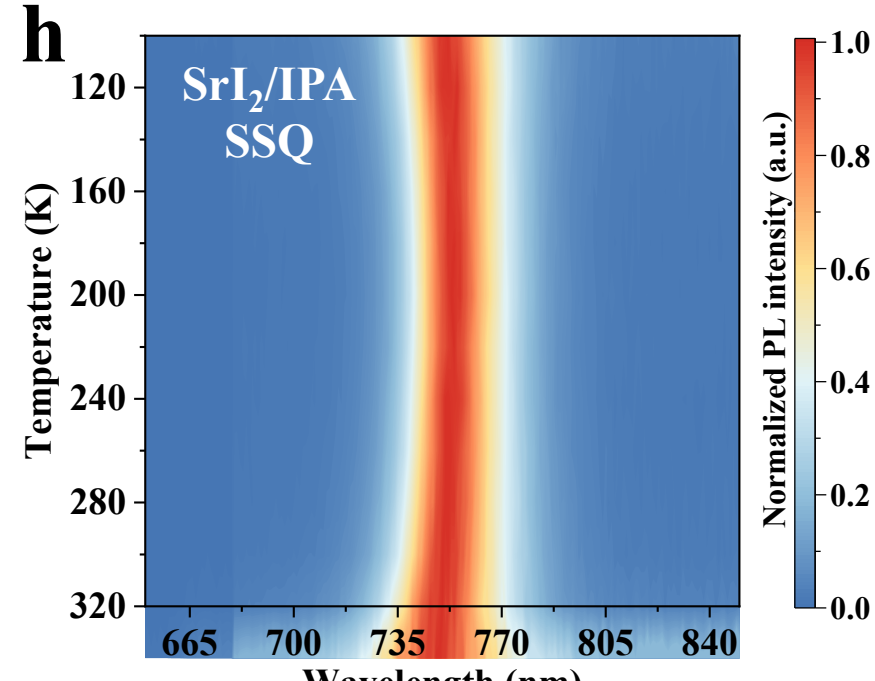
h
SrI2/IPA SSQ
Temperature (K)
Wavelength (nm)
Normalized PL intensity (a.u.)

a
control
α_i = 2.0°
b
control
α_i = 1.5°
c
control
α_i = 1.0°
d
SrI2/IPA SC
α_i = 2.0°
e
SrI2/IPA SC
α_i = 1.5°
f
SrI2/IPA SC
α_i = 1.0°
g
SrI2/IPA SSQ
α_i = 2.0°
h
SrI2/IPA SSQ
α_i = 1.5°
i
SrI2/IPA SSQ
α_i = 1.0°
q_z (Å^{-1})
q_{xy} (Å^{-1})
Intensity (a.u.)
100
1
j
k
l
control
SrI2/IPA SC
SrI2/IPA SSQ
Ψ = 45°
Ψ = 35°
Ψ = 25°
Ψ = 15°
Ψ = 5°
Normalized intensity (a.u.)
2θ (°)
m
control
SrI2/IPA SC
SrI2/IPA SSQ
slope = -0.13
slope = -0.09
slope = -0.11
2θ (degree)
sin$^2\psi$
n
SrI2/IPA spin-coating
SrI2/IPA quenching
Control
δ_R = 51.76 Mpa
δ_R = 44.68 Mpa
δ_R = 36.83 Mpa
Tensile stress release

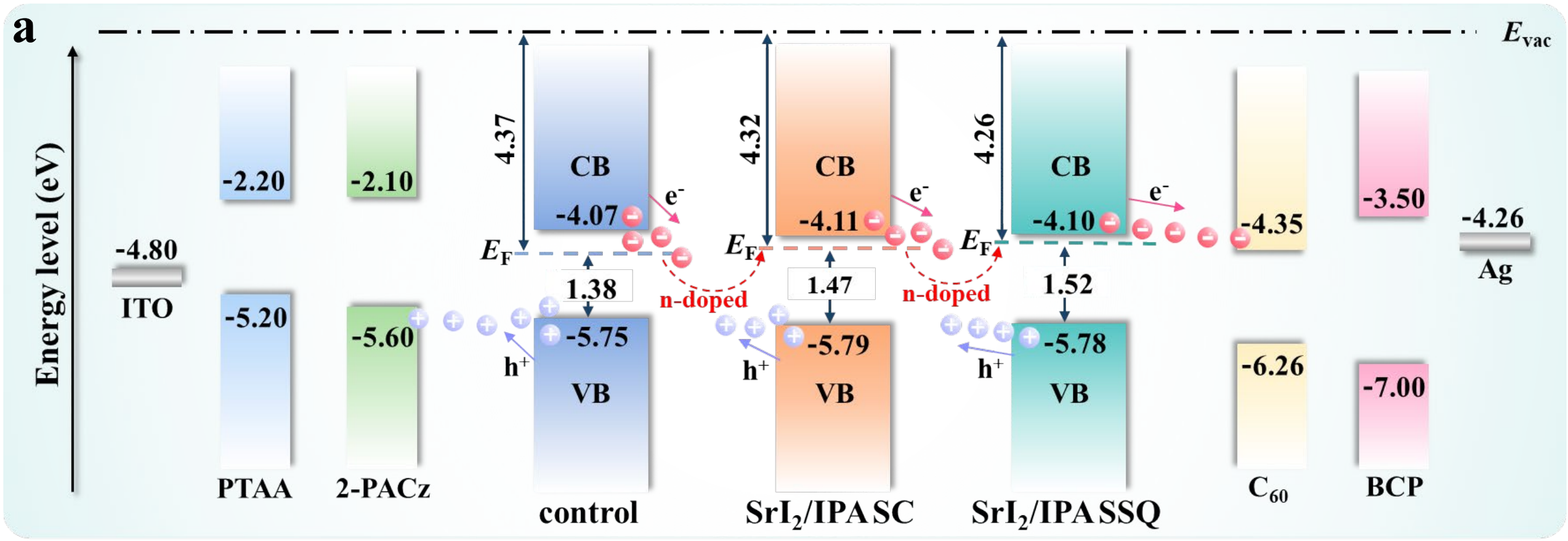
a
E_{vac}
Energy level (eV)
-4.80
ITO
-2.20
-5.20
PTAA
-2.10
-5.60
2-PACz
4.37
CB
-4.07
E_F
1.38
-5.75
VB
control
4.32
CB
-4.11
E_F
1.47
-5.79
VB
SrI_2/IPA SC
4.26
CB
-4.10
E_F
1.52
-5.78
VB
SrI_2/IPA SSQ
e⁻
h⁺
n-doped
-4.35
C_{60}
-6.26
-3.50
BCP
-7.00
-4.26
Ag

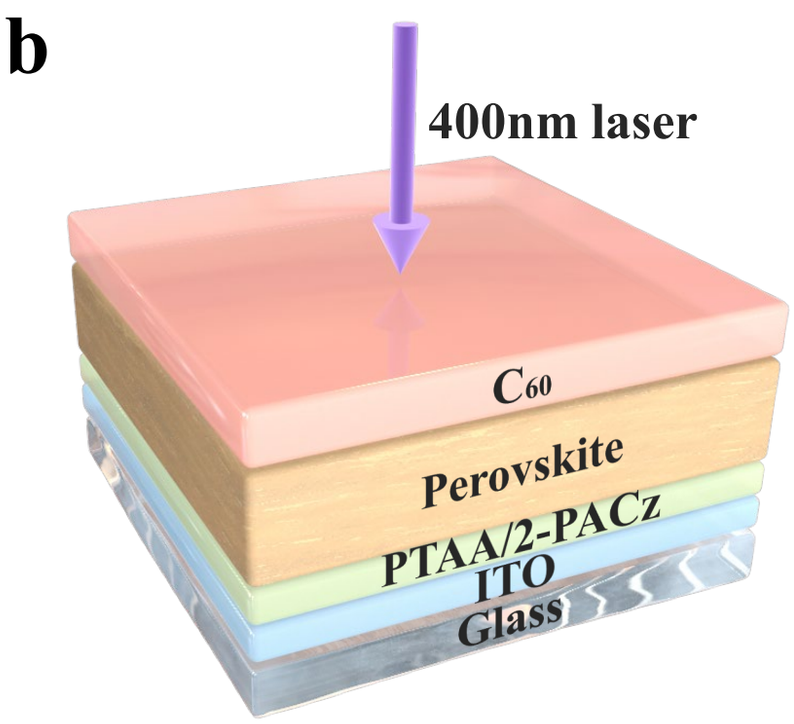
b
400nm laser
C_{60}
Perovskite
PTAA/2-PACz
ITO
Glass

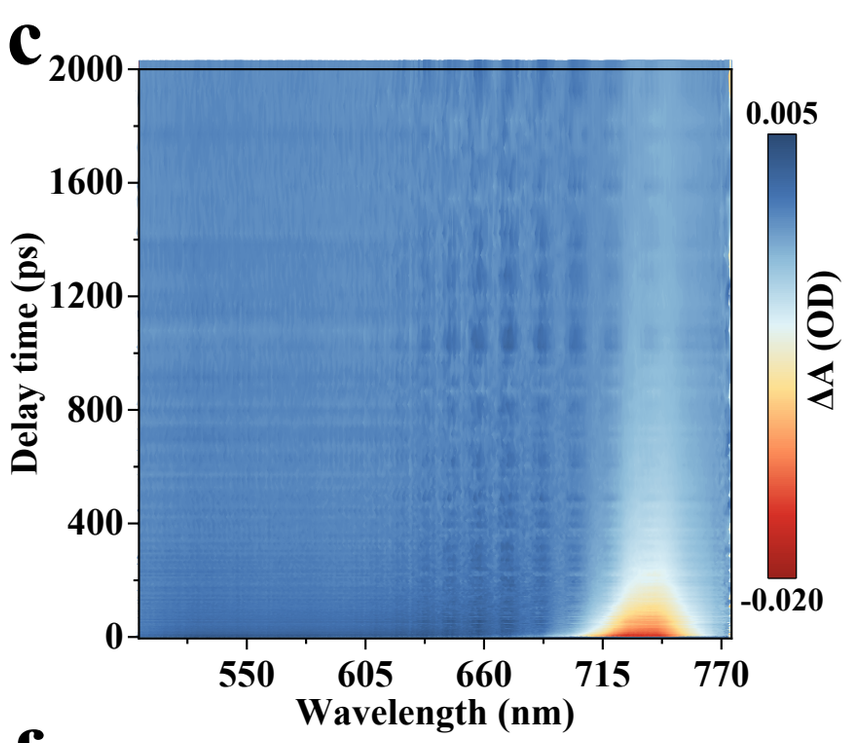
c
Delay time (ps)
2000
1600
1200
800
400
0
550
605
660
715
770
Wavelength (nm)
0.005
-0.020
ΔA (OD)

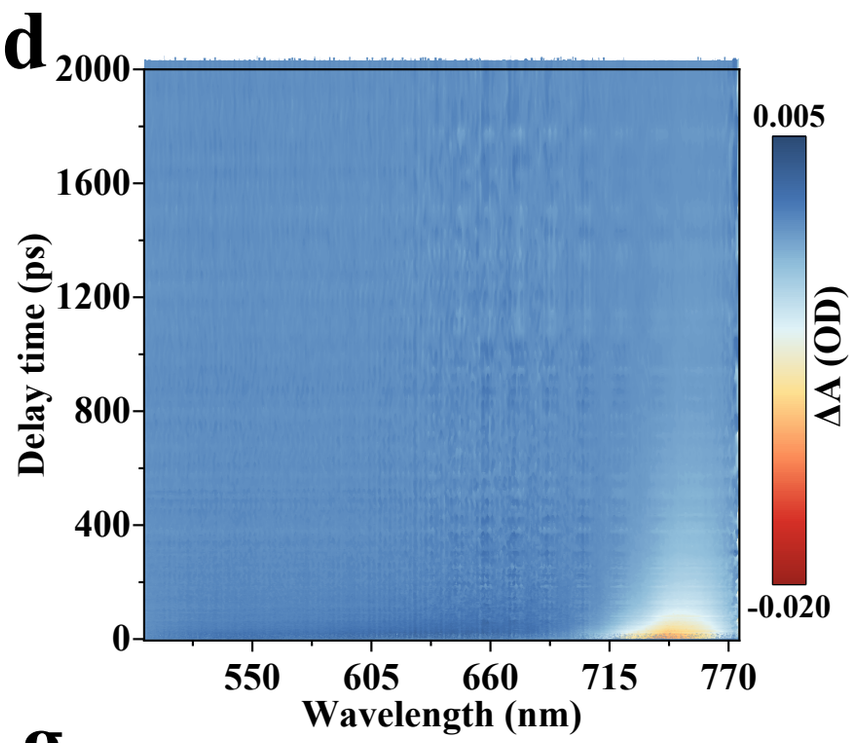
d
Delay time (ps)
2000
1600
1200
800
400
0
550
605
660
715
770
Wavelength (nm)
0.005
-0.020
ΔA (OD)

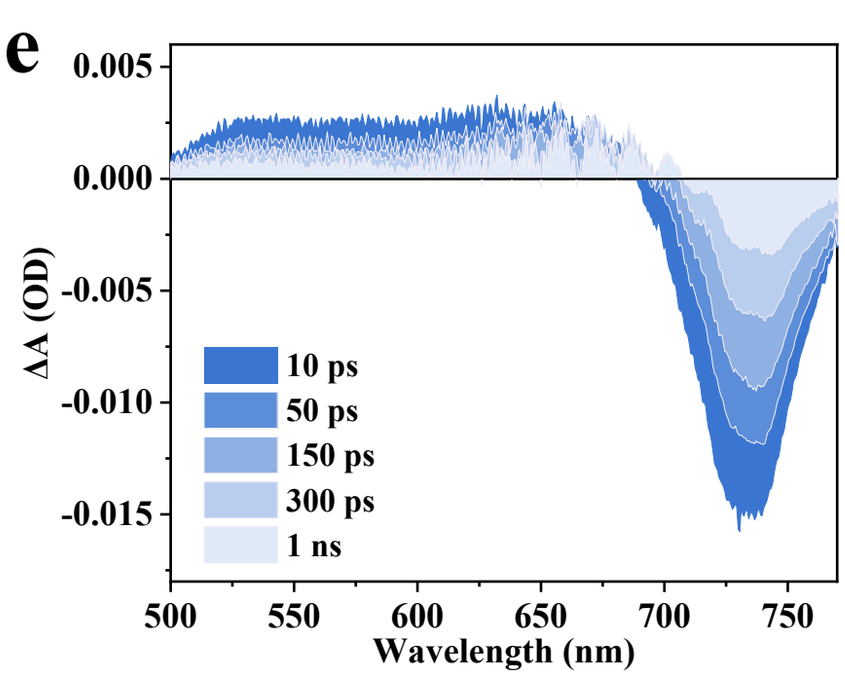
e
ΔA (OD)
0.005
0.000
-0.005
-0.010
-0.015
10 ps
50 ps
150 ps
300 ps
1 ns
500
550
600
650
700
750
Wavelength (nm)

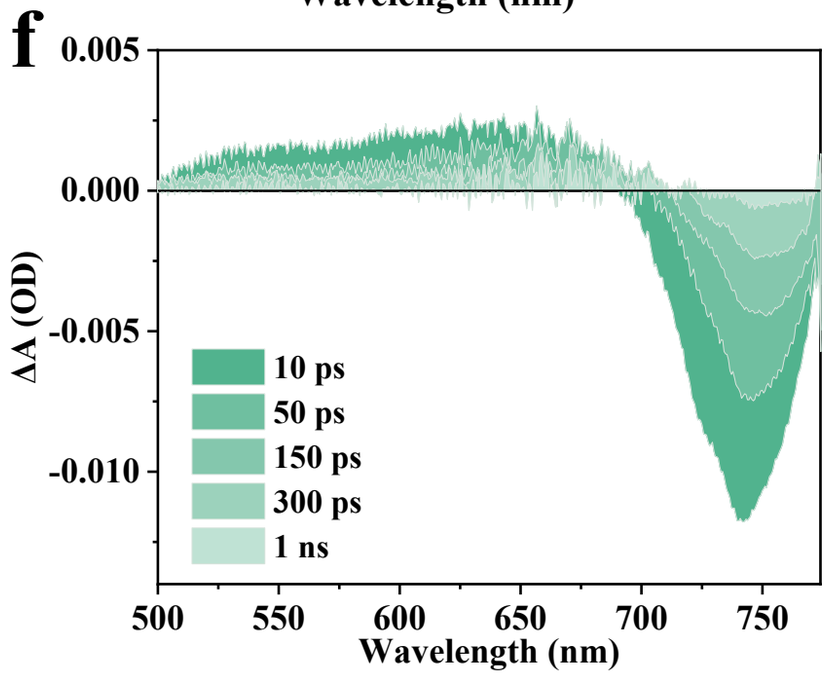
f
ΔA (OD)
0.005
0.000
-0.005
-0.010
10 ps
50 ps
150 ps
300 ps
1 ns
500
550
600
650
700
750
Wavelength (nm)

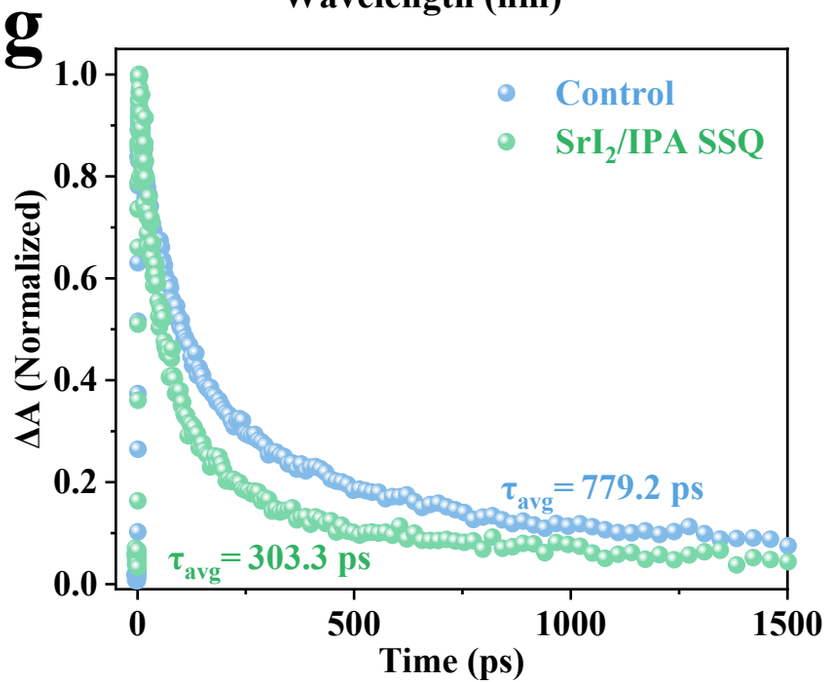
g
ΔA (Normalized)
1.0
0.8
0.6
0.4
0.2
0.0
Control
SrI_2/IPA SSQ
τ_{avg} = 779.2 ps
τ_{avg} = 303.3 ps
0
500
1000
1500
Time (ps)

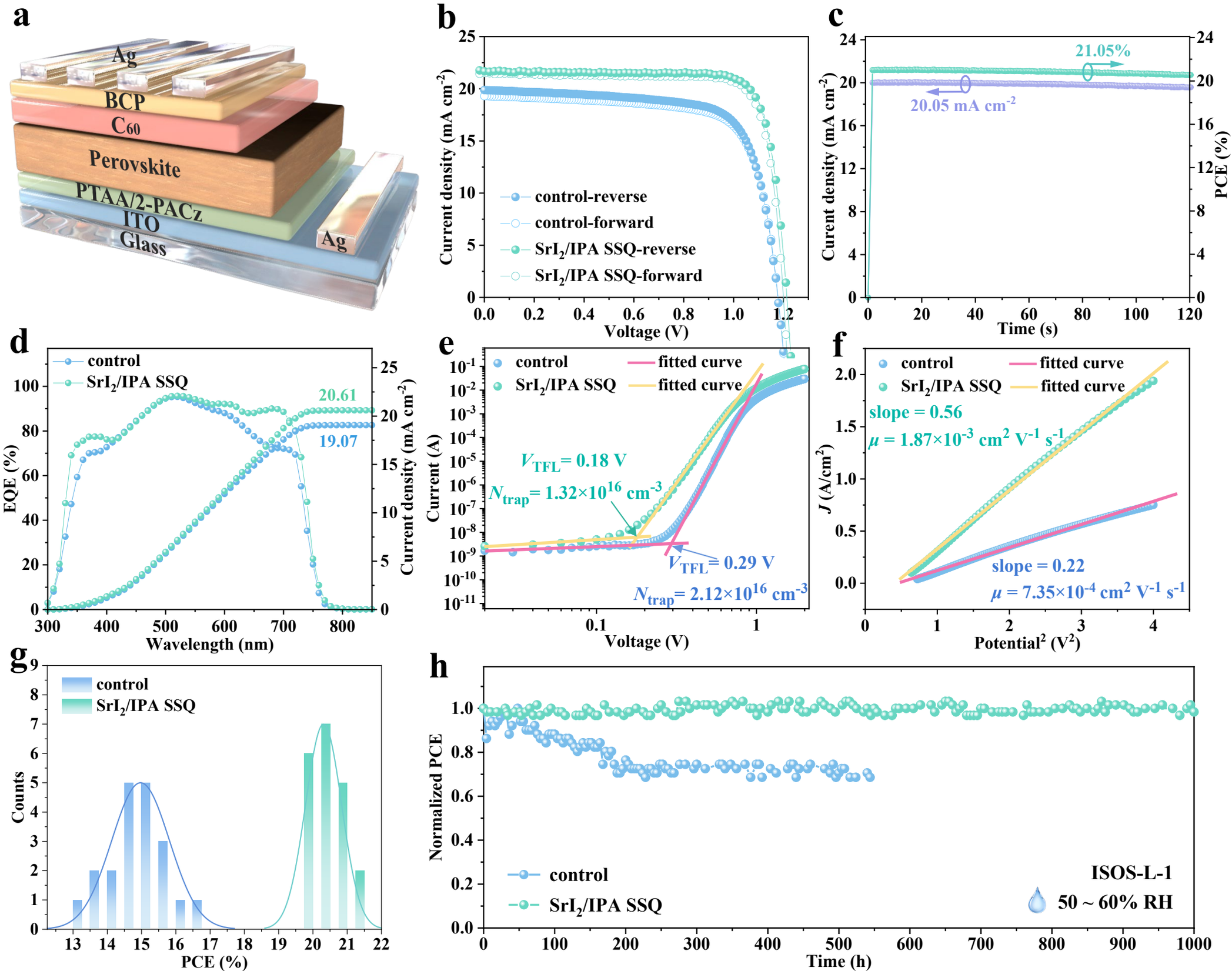
a
Ag
BCP
C60
Perovskite
PTAA/2-PACz
ITO
Glass
Ag
b
Current density (mA cm-2)
Voltage (V)
control-reverse
control-forward
SrI2/IPA SSQ-reverse
SrI2/IPA SSQ-forward
c
Curent density (mA cm-2)
PCE (%)
Time (s)
21.05%
20.05 mA cm-2
d
EQE (%)
Current density (mA cm-2)
Wavelength (nm)
control
SrI2/IPA SSQ
20.61
19.07
e
Current (A)
Voltage (V)
control
SrI2/IPA SSQ
fitted curve
fitted curve
VTFL= 0.18 V
Ntrap= 1.32×10^16 cm-3
VTFL= 0.29 V
Ntrap= 2.12×10^16 cm-3
f
J (A/cm2)
Potential2 (V2)
control
SrI2/IPA SSQ
fitted curve
fitted curve
slope = 0.56
μ = 1.87×10-3 cm2 V-1 s-1
slope = 0.22
μ = 7.35×10-4 cm2 V-1 s-1
g
Counts
PCE (%)
control
SrI2/IPA SSQ
h
Normalized PCE
Time (h)
control
SrI2/IPA SSQ
ISOS-L-1
50 ~ 60% RH

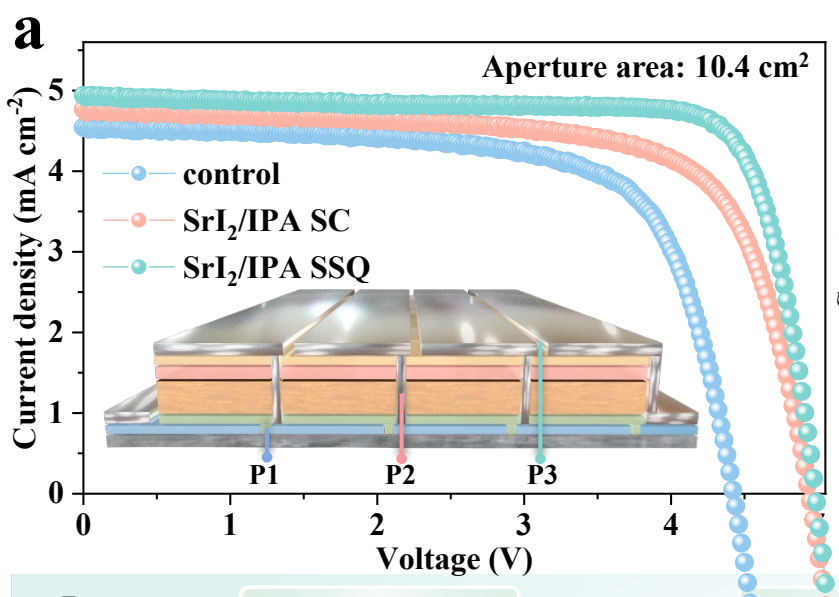
a
Aperture area: 10.4 cm²
control
SrI2/IPA SC
SrI2/IPA SSQ
P1
P2
P3
Current density (mA cm⁻²)
Voltage (V)

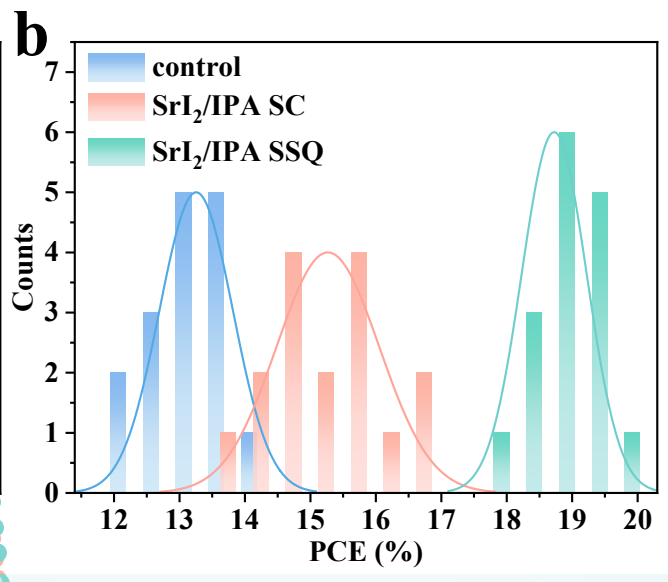
b
control
SrI2/IPA SC
SrI2/IPA SSQ
Counts
PCE (%)

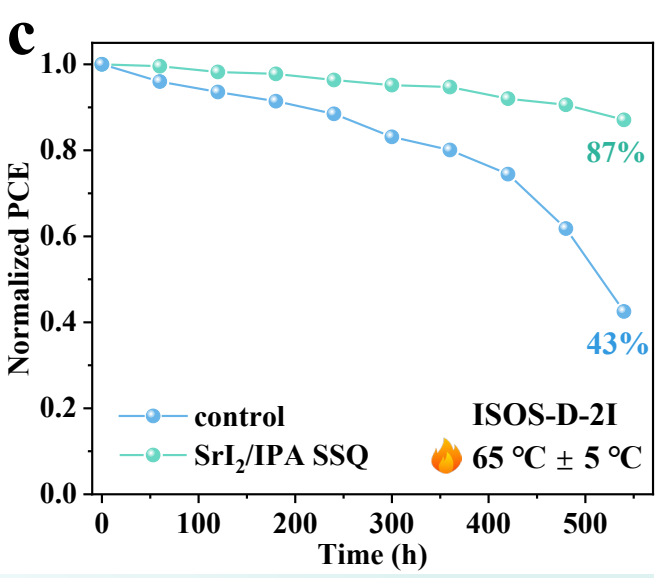
c
87%
43%
control
SrI2/IPA SSQ
ISOS-D-2I
65 °C ± 5 °C
Normalized PCE
Time (h)

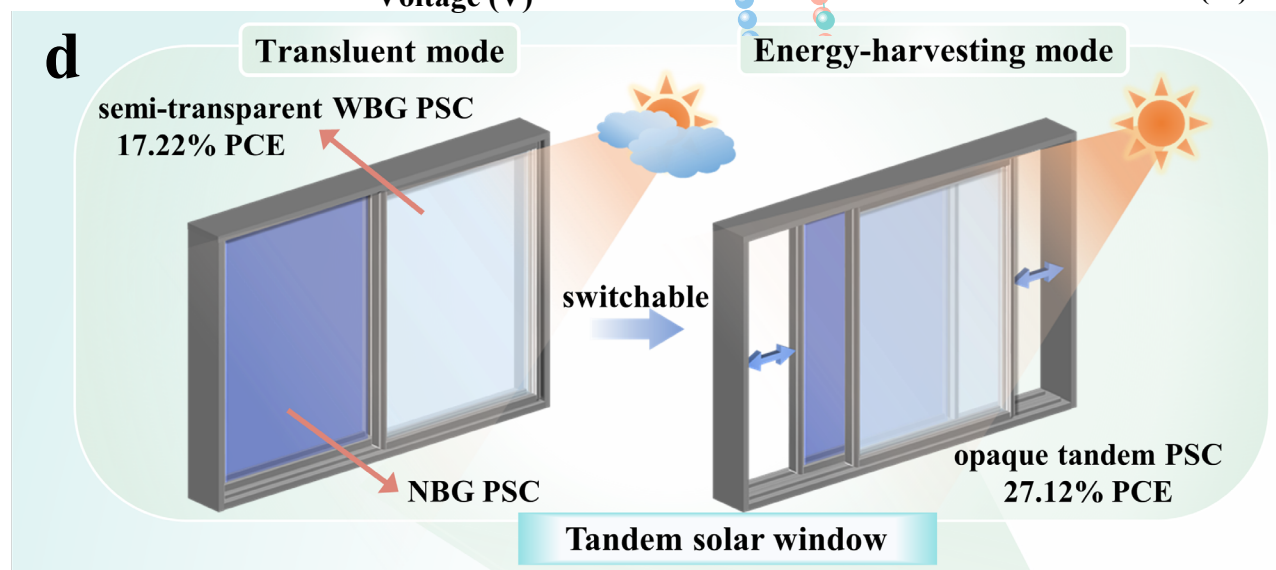
d
Transluent mode
Energy-harvesting mode
semi-transparent WBG PSC
17.22% PCE
switchable
NBG PSC
opaque tandem PSC
27.12% PCE
Tandem solar window

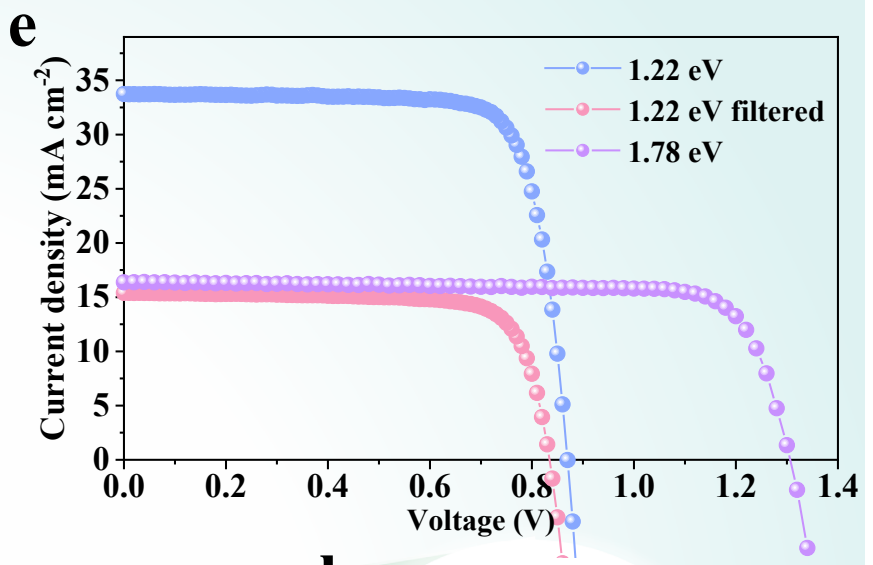
e
1.22 eV
1.22 eV filtered
1.78 eV
Current density (mA cm⁻²)
Voltage (V)

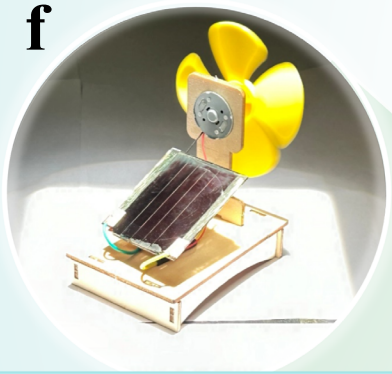
f
PSM-powered desktop fan

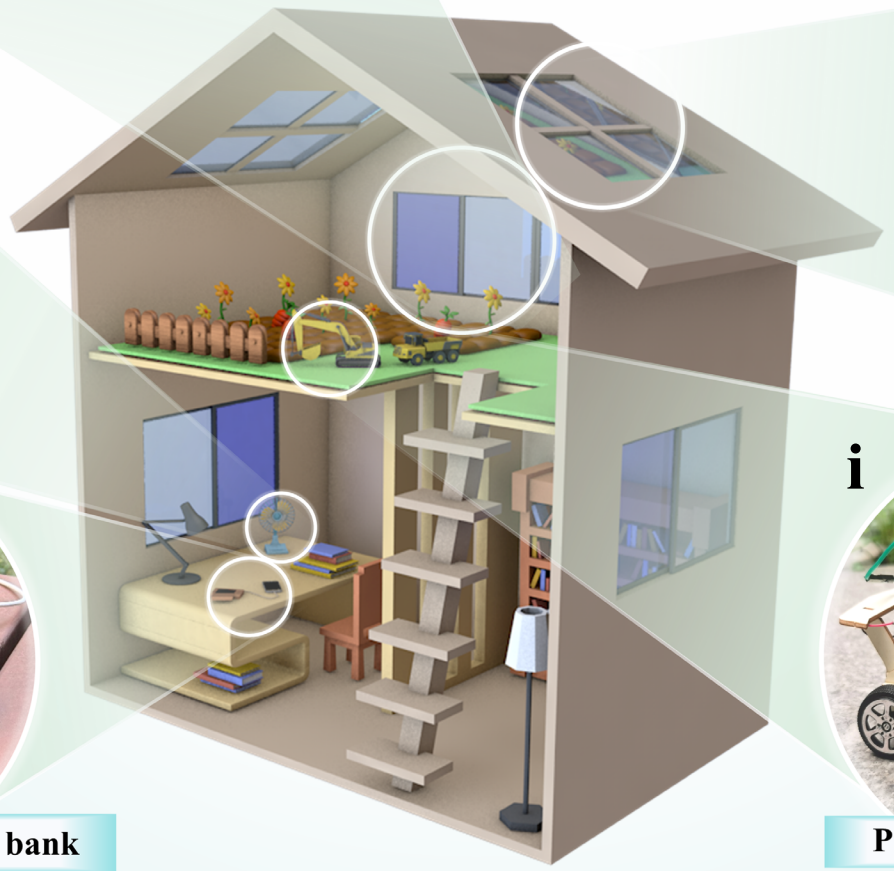


h
bifacial ηeq = 18.41%
Semi-transparent photovoltaic window

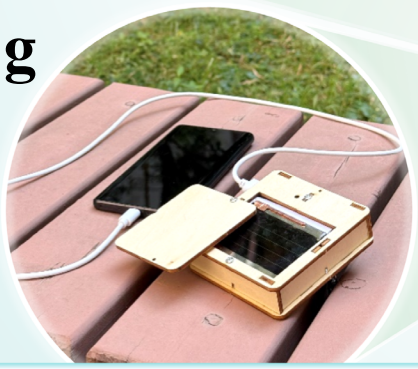
g
PSM-driven portable power bank


i
PSM-powered tool car